scientific reports

Check for updates

OPEN

# Telecommunication-inspired network models of healthy and diseased brains

Peppino Fazio[1,2]✉, Maria Mannone[1,3,4,5], Norbert Marwan[4,5], Patrizia Ribino[3], Miralem Mehic[2,6], Abdalla Swikir[7], Danilo Amendola[8], Pietro Riello[1] & Miroslav Voznak[2]

**Recent advances in nanoelectronics have spurred increased interest in the human brain and its complex functions. Numerous studies have explored brain behavior in varying levels of detail, from individual neurons to entire lobes. Intricately structured, the brain is a complex organ susceptible to diseases that may disrupt the connectivity between its internal regions. Investigating this phenomenon, the present study applies a discrete finite-state model to map the behavior of neurons within a neuronal agglomerate and examine the effect of disease on these behaviors. Each agglomerate is then compared to a wireless clustered network and modeled as a finite-state system, with inter-cluster communications analyzed under conditions of temporal variations and degradation. This work represents one of the most advanced applications of discrete finite-state processes and routing theory in brain modeling.**

**Keywords** Biological neural network, Biological routing, Channel modeling, Communication theory, Finite state process

A small unit capable of transforming into any cell type: such is the remarkable nature of stem cells. The transformative ability of these cells has attracted great interest across scientific disciplines and driven research toward the development of innovative treatment strategies. Originating at the cellular level, the brain's intricate workings and neuronal interactions shape human cognitive processes. The recent surging interest in neuronal cell behavior has been largely driven by work to replicate the biological models of humans and other animals from their fundamental components, such as cells, molecules, and organs[1,2]. The development of a comprehensive, detailed model of the brain is also essential in understanding neurological diseases and predicting their biological effects. In this research area, many of the studied critical brain processes, both normal and pathological, occur at the mesoscopic scale between the level of single neurons and the entire brain[3].

Widely recognized for his seminal contributions to brain mapping, Korbinian Brodmann[4] and his research provided early evidence that the brain does not function as a single, unified entity but instead assigns cognitive tasks to specialized regions, highlighting the distributed nature of brain functions. Connectivity is central to brain function; it is therefore intuitive to model the brain as a network in which brain regions act as nodes and their anatomical or functional connections behave as links[5]. Neuroscience research has demonstrated that brain networks vary across individuals and evolve over time. Comparative analyses show that structural and functional brain networks differ between healthy individuals and those with neurological conditions[6] and also change throughout an individual's lifetime[7].

Given that the brain functions as a complex network of structurally and functionally interconnected regions, communication between these regions provides essential support to higher cognitive processes that depend on the continuous integration of information across brain areas. Consequently, the study of functional connectivity in the brain can yield valuable insights into the organ's fundamental structure.

The primary non-invasive, informative methods for examining brain network activity are diffusion magnetic resonance imaging (MRI), functional MRI (fMRI), and EEG/MEG recording[8].

[1]DSMN, Ca' Foscari University of Venice, Via Torino 155, 30170 Mestre (VE), Italy. [2]Department of Telecommunications, VSB - Technical University of Ostrava, 17. listopadu 15, 70800 Ostrava, Czechia. [3]ICAR, National Research Council (CNR), Palermo, Italy. [4]Potsdam Institute for Climate Impact Research (PIK), Member of the Leibniz Association, Berlin, Germany. [5]Institute of Physics and Astronomy, University of Potsdam, Potsdam, Germany. [6]Department of Telecommunications, Faculty of Electrical Engineering, University of Sarajevo, Sarajevo, Bosnia and Herzegovina. [7]Mohamed bin Zayed University of Artificial Intelligence (MBZUAI), Abu Dhabi, UAE. [8]Joint Research Centre, European Commission, Rue du Champ de Mars 21, 1050 Brussels, Belgium. ✉email: peppino.fazio@vsb.cz; peppino.fazio@unive.it

Functional connectivity refers to the temporal correlation between neurophysiological events occurring in different brain regions. In neuroimaging, this typically involves temporal correlations in cerebral blood flow or blood oxygen level dependent (BOLD) signals[9]. Functional connectivity is often assessed by measuring the co-activation of spontaneous fMRI time series obtained during resting states. Regions of interest (RoIs) serve as the nodes of functional brain networks, each RoI comprising several fMRI measurement voxels presumed to be functionally related.

Advancements in brain modeling not only provide crucial support to medical and biological research but also inform the design of information and communication technologies (ICTs). Comprehension and representation of the brain's intricate neuronal networks can assist the development of advanced algorithms and systems for data transmission and processing[10–12]. Neural network models inspired by the brain's architecture can also enhance machine learning methods in telecommunications to effect improvements in signal processing, error correction, and data compression. Insights into brain connectivity and communication pathways may also guide the design of more efficient and resilient communication networks that mirror the brain's ability to rapidly and reliably transmit information across extensive neural circuits. This interdisciplinary approach is expected to drive innovations that will transform both neuroscience and telecommunications and lead to smarter, more adaptive, and more efficient technologies.

Based on these observations, we conducted a theoretical and experimental study to develop a model describing the behavior of neuronal agglomerates in the brains (specifically within RoIs) of both healthy individuals and individuals affected by a neurological disease. Our study is a proof of concept of a new approach toward functional brain activity modeled as a telecommunication network. We present the theoretical idea, the network protocol, and our results obtained from fMRI data of selected patients. The study starts with the retrieval of fMRI voxel images stored in *DICOM* files[13] in the ADNI dataset[14]. The voxels were then grouped according to specific brain parcellations, according to a selected brain atlas(Several RoI classifications (atlases), which differ in the number, size, and distribution of RoIs based on their intended application and brain segmentation methodology, are available. Examples include the Fornix[15], Harvard-Oxford[16], Julich-Brain Cytoarchitectonic[17], HCP Probabilistic Tract[18] atlases.). After application of the atlas-specific mask, the time series corresponding to the signals emitted by the designated brain areas were extracted, forming a time series for each RoI. Stored in (Neuroimaging Informatics Technology Initiative) NIfTI files[19,20], the time series data provide detailed information about each RoI's dynamics over time[21]. Computation of the correlations between time series also permits the derivation of a connectivity matrix[22]; the present study, however, focuses primarily on time series. At this stage, the temporal evolution of each RoI was modeled through a **Finite State Agglomerate Process (FSAP)**, and the effects of disease were analyzed for behavioral changes occurring within each RoI.

The article's second main contribution is the introduction of an **inter-RoI communication model** that maps functional communication channels between RoIs by quantifying the correlations in their fMRI time series dynamics. In this model, RoIs are treated as data sources and destinations, and their connections are represented as classic dynamic channels. This approach enables the characterization of brain activity as a simplified network, facilitating comparisons between healthy and diseased states. Furthermore, unlike traditional static global analysis, the model incorporates dynamic temporal analysis to capture time-dependent variations in brain function. Even when only resting-state fMRI is considered, changes in brain activity, particularly during rest (within the default mode network) can vary according to specific neuropsychiatric diseases[23]. The present study focuses on resting-state fMRI data, comparing healthy brains with the brains of patients affected by Alzheimer's disease (AD), better denoted as *Alzheimer–Perusini's disease* for historical reasons[24].

The remainder of the article is structured as follows: Section 2 gives a wide overview of the related work, Section 3 presents the proposed model; Section 4 outlines preliminary findings and details some data experiments; Section 5 concludes the article with a discussion of future directions for research.

## Related work

There is extensive literature on analyzing human data regarding the damage neurological diseases inflict on neurons and entire brain networks, both anatomical and functional.

The first refers to the system of nodes and connections, as stations (nodes) and highways (links) between them. The second refers to the information exchange between nodes through the links across the pathways. Neurological problems can often be described as damage to nodes or highways. The functional network analysis, which can be recovered through fMRI, provides information on the connectivity between brain regions and can signal the presence of a disease. While there are distinctions between the brain networks of females and males, as well as younger and older individuals, one can nevertheless identify the characteristic marks of diseases.

Alterations induced by disease or surgery can have a disastrous impact on pathways. Effects include the incapability of a person to recognize faces (*prosopagnosia*)[25], or the apraxia and aphasia occurring in the *disconnection syndrome*[26]. The investigation can focus on the brain regions with high connectivity, found among the brain's most efficient pathways[27], the so-called *hubs*[8]. Increased synchronization characterizes, for instance, the alteration occurring in epilepsy[8]. The randomization of weights of specific brain regions particularly characterizes schizophrenia[28].

Moreover, recent neuroimaging studies have introduced the hypothesis that widespread disruptions in brain connectivity may account for the diverse range of behavioral impairments observed in individuals with autism[29].

Based on neuroimaging findings, Just et al.[30] proposed the underconnectivity theory, linking autism-related behaviors to reduced communication between frontal and posterior brain regions, affecting tasks requiring their coordination. Similarly, resting-state studies in individuals with strabismus reveal network abnormalities. Kang Yu et al.[31] observed increased activity in visual and sensorimotor networks, while Jin[32] found disruptions in cerebellar, sensorimotor, visual, and auditory networks in patients with concomitant exotropia.

Finally, for Alzheimer's disease (AD), there is a progressive destruction of neurons, which can be thought of as the progressive interruption of communication between them, with repercussions at the level of the brain network[33]. Comparing healthy individuals and AD patients, it has been found that the latter presents a diminution of the strength of long links (between distant parts of the brain) and an increase in the strength of short links[34].

Hence, it is evident that neuropsychological diseases can be better understood through advanced brain modeling techniques, which simulate brain networks to explore the underlying cognitive and neurological dysfunctions. Recent studies suggest that a comprehensive model of brain networks and their damage could offer a unified perspective on these diseases and support the development of future treatments[35].

The study in[36] addresses brain shift, a key challenge in deep brain stimulation (DBS) surgeries where brain tissue movement can affect the precise placement of electrodes, crucial for treatment effectiveness. In[37], authors apply deep learning to estimate brain strain—deformation of brain tissue vital for understanding traumatic brain injuries (TBIs) and other neurological disorders. These deep learning models enable fast and accurate strain assessment, offering significant improvements in diagnosing and treating TBIs. Together, these works highlight advances in neurosurgery and brain injury assessment, emphasizing the role of technology in enhancing patient outcomes.

The work presented in[38] proposes a method for matching up large-scale maps of brain tissue with tiny details about individual molecules within the brain, mainly focusing on 2D slices, using mathematical techniques. This alignment helps researchers understand how molecular details relate to the brain's overall structure.

The study proposed in[39] explores how individual differences in brain networks manifest. The study identifies two primary types of variation: boundary shifts between adjacent brain regions and ectopic intrusions, where differences appear in unexpected locations. These findings challenge previous assumptions that individual brain differences are mainly due to border shifts. Understanding these variations helps in predicting cognitive abilities, explaining behavioral differences, and identifying biomarkers for brain disorders.

Given such a connection with the mathematical formalization of networks, one can wonder about the role of mathematics in a more general neuro-pathological depiction.

Mathematical models of neural agglomerates have compared neurons to springs with threshold-based interactions[40,41]. A top-down approach to brain disease, using multi-layer brain networks, was introduced in[42], while in[43] two key contributions were presented: a matrix-based model of brain networks altered by a mathematical operator, and a channel model describing healthy or disrupted communication between neurons and neuronal masses.

Building on previous research, and in particular on[42], here we propose an innovative idea for brain modeling drawing from networking and wireless/wired communications methodologies[44–47] to model neuronal agglomerates and their inter-communication. Particularly, the main novel contributions of this work are:

- Starting from fMRI (DICOM) and NIfTI data (time series), the FSAP model is proposed for describing the behavior of each RoI (node) in terms of discrete states and transition probabilities between states;
- Intra-node data (time series) correlation is studied to make a comparison between healthy and diseased brain; it is worth noting that the proposed approach is completely general, although we use data from AD patients.
- In addition to the NIfTI correlation analysis, the parameters of the FSAP are also studied to establish a relationship between healthy and diseased models;
- Different from the existing literature, inter-node interaction is also one of the main results that will be analyzed. In addition to nodes (neuronal agglomerates or RoIs), the links between nodes (edges) are considered, having the chance to model the whole system as a dynamic telecommunication network, where signals are transmitted through fading/degraded channels. Typical computer network performance parameters are then considered for deep analysis and comparison between a healthy and a diseased brain.

To the best of our knowledge, the human brain has never been compared with a clustered telecommunication network with faded/degraded channels, where each node represents a source and/or a receiver of information. The existing literature is limited to a complex graph representation of the brain in terms of RoIs and correlations between RoIs. No further investigations are made from a different point of view.

In patients with AD, progressive neuronal degradation leads to disrupted neural communication, affecting overall brain network connectivity[33]. Studies show that AD patients experience a reduction in long-range connectivity (between distant parts of the brain) and an increase in short-range connectivity[34].

In view of this network-based perspective, examining the broader role of mathematical modeling in the characterization of neurodegenerative diseases can provide valuable insight.

For example, the authors of[40] explore mathematical models of neural agglomerates, representing neurons as springs whose extension corresponds to activation thresholds. In[41], neuronal interactions are modeled as multiple threshold units. A top-down, overall mathematical framework for brain diseases, based on multi-layer brain networks[43], is proposed in[42].

To our knowledge, existing literature primarily represents the brain as a graph based on RoIs and their correlations, without exploration of alternative perspectives. Building on this body of research, and particularly on the work in[42], the present study proposes an innovative brain modeling approach that draws from networking and wireless/wired communication methodologies[44–47].

## Methods: the human brain as a telecommunication network

This section presents the main proposal, which aims to model the human brain as a telecommunications network, and to analyze its performance in healthy and diseased conditions.

We did not implement the data acquisition by ourselves; our study used publicly and freely available data from the ADNI repository. ADNI would grant the research team access to the data for download through their website[48]. More details about the ADNI project and data acquisition, and sharing policies and protocol can be found at[49]. The generalization of the main steps of the proposed approach are shown in Figure 1. The process starts from the top-left corner, with the choice of a brain atlas, which gives a precise brain parcellation so, moving down in the figure, a node of a graph can be immediately associated to each RoI. By taking as input also the fMRI dataset from ADNI, moving right from top-left of the figure, a time series representation of RoIs activities can be obtained, by data conversion of DICOM to NIfTI formats. At this point, following the pipeline, temporal data is quantized, giving the possibility to obtain the FSAP for each RoI (intra-RoI model). By applying the mutual information approach the dynamic weights for the graph can be evaluated through the adjacency matrix, giving to the telecommunication model the missing knowledge regarding the edge weights over time. The code to extract time series from fMRI can be accessed at https://codeberg.org/medusamedusa/time_series_from_AD_fMRI_.

In other words, in this article, we schematize the functional connectivity of the brain via the paradigm of telecommunications: a system of nodes and links between them, that receive and send information, traveling across the links. The details of the proposed model will be discussed in the next sub-sections. Here we propose, instead, the theoretical background where our approach can be framed.

The basic unit of brain activity is given by neuronal firing. A neuron is a cell that receives chemical signals at its dendrites, which generate electrical changes in the membrane. These signals are integrated in the soma and axon hillock. If the membrane potential reaches a threshold, an action potential is generated and propagates along the axon, leading to neurotransmitter release at the synapses—the neuron *fires*.

We distinguish between excitatory neurons and inhibitory neurons, a difference that should be preserved in biologically-plausible models of brain networks, according to the Dale's law[40,50]. Choosing one typology, for the sake of simplicity, following[40] we can write down the potential of the $i$-th neuron at time $t$:

$$F_i(t) = \sum_j w_{ij} f(x_j), \tag{1}$$

where $x_j(t)$ is the incoming signal, $w_{ij}$ is its weight, and $f$ is the activation function. The neuron fires when the threshold is reached. Multiple neurons constitute a *neuronal population*, or a neural mass. From Eq. (1), we can build the potential of a neural mass[40]:

$$E(t) = \sum_{i^+} F_i(t), \tag{2}$$

with + denoting the excitatory neurons. As proposed in[42], we can see neural masses as the nodes of a network, with weights of the links representing the strengths of the anatomic and functional connections between them.

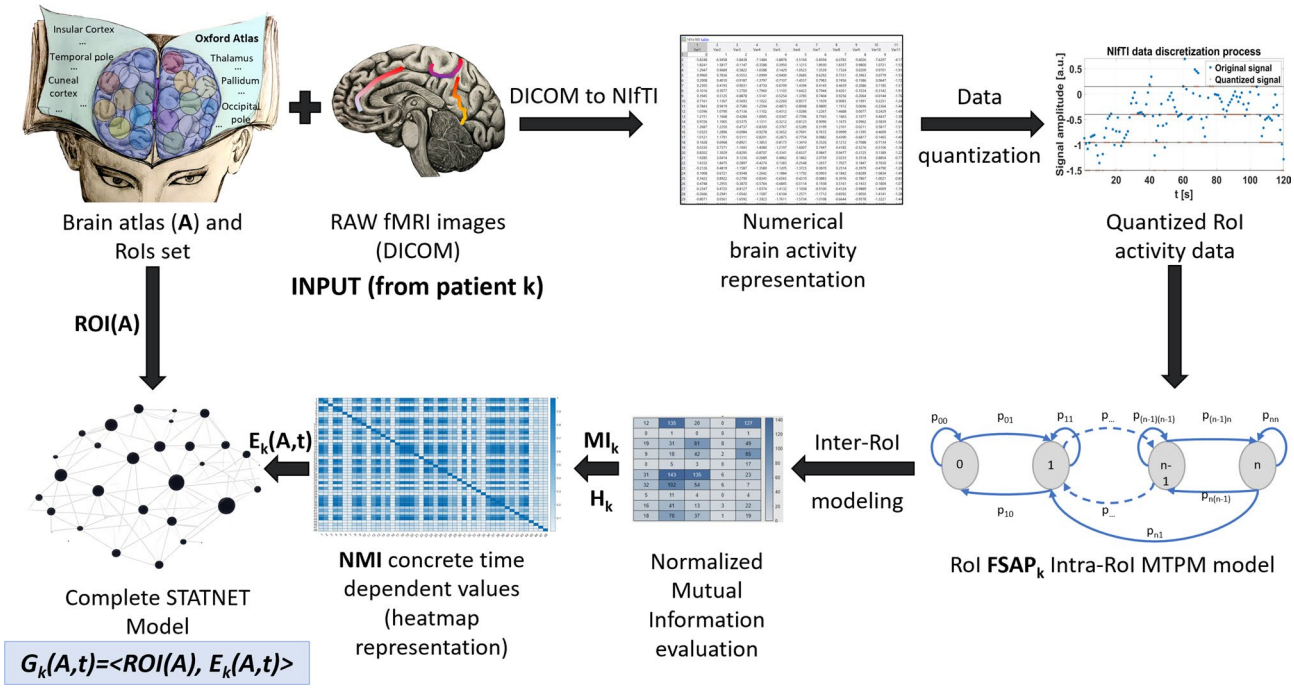


**Fig. 1**. The complete pipeline of the proposed FSAP and static telecommunication model (image created via PowerPoint from Microsoft 365 Suite, with hand-made pencil drawings by Maria Mannone).

Thus, if we identify a neuronal population with a node, from Eq. (2) we can compute the potential of a macro-area:

$$E^l = \sum_z \mathcal{W}_z^l E_z^l(t), \tag{3}$$

where we consider the $l$-th lobe of the brain, the $z$-th node in each lobe, the weights $\frac{l}{z}$ of the $z$-th node in the $l$-th lobe, and finally, the potential $E_z^l$ of each node, which can be expressed as follows[42]:

$$E_z^l(t) = \sum_{i^+} F_i^{l,z}(t) = \sum_{i^+} \sum_j w_{ij}^{l,z}(x_j). \tag{4}$$

Neurological disorders can alter the weights $w_{ij}^{l,z}$, as well as surgeries, and use of toxic substances. The alteration of weights between neuronal connections, if higher than a certain extent, can impact the functioning of the overall neuronal mass to which the neurons belong. For instance, the death of an entire neuronal mass, from a telecommunication point of view, is the same thing as shutting down a source of signal. This appears as being equivalent to cutting all connections between the population and the rest of the brain. Thus, there are anatomic alterations that can heavily impact the functional working of the brain. That is, a disruption of the roads of communications obviously leads to disruptions also in the traffic of information through them. However, also an impact anatomic connection (a non-disrupted anatomic pathway) can present an altered traffic.

We focus here on functional connectivity of the brain. We can describe several neurological diseases in terms of alterations of the functional connectivity of the brain[9,22,30,34]. The study[42] also includes a first toy model of alteration of neuronal firing in terms of a disrupted channel model. Here, we unfold this intuition, analyzing in a great detail the channel-like functioning of normal brains, and the alterations occurring in a degenerative disorder. Also, we directly focus on populations as "overall entities", neglecting the level of single neurons.

This section is structured as follows:

- Subsection "The theoretical FSAP for Brain RoIs Modeling" gives an introductory description of the main proposed idea, in terms of brain graph association through the application of atlas parcellation;
- Subsection "Time Series Discretization, RoI States and Interactions: a deep theoretical analysis" shows how it possible to apply a discretization approach to fMRI values, in order to reach an approximation of RoI states and associated values;
- Subsection "From Brain Activity to Networking" concludes the theoretical proposal by considering the brain activities as traffic flows inside a telecommunication network.

## The theoretical FSAP for brain RoIs modeling

Before introduction of the model, we revisit the definitions of brain atlases and RoIs, even though they are already well established concepts.

A brain atlas is a detailed, comprehensive map of the brain's anatomy, and in some cases, its functional areas. It serves as an essential reference in understanding the brain's structure and organization. Brain atlases are used widely in neuroscience research, clinical practice, and education for the study and interpretation of brain function and pathology[51,52]. Each atlas provides an indexed set of RoIs.

An RoI in neuroimaging and neuroscience research refers to a specific area within the brain. RoIs are used to isolate and examine particular brain regions based on their structure, function, or response to stimuli[53], as defined by a given atlas.

For an atlas $A$, the set of RoIs can be expressed as:

$$RoI(A) = \{r_1^A, r_2^A, ..., r_{n_A}^A\}, \tag{5}$$

where $|RoI(A)| = n_A$, indicating that the number of RoIs (parcellations) depends on the selected atlas. Each RoI $r_i^A \in RoI(A)$ comprises a large number of neurons:

$$r_i^A = \{n_{i1}^A, n_{i2}^A, n_{ij}^A, ..., n_{in_i^A}^A\}, \tag{6}$$

where $|r_i^A| = n_i^A$. Here, the scales of $n_A$ and $n_i^A$ differ greatly (the number of functional RoIs in a brain is in the order of tens, whereas each RoI contains billions of neurons).

We now introduce edges between the RoIs. Initially, a mesh topology is assumed for the RoI nodes $RoI(A)$. Using concrete fMRI data, the weights of these edges can be determined from observed interactions within the brain connectome. If no interaction exists between two RoIs, the corresponding edge has a zero weight, effectively removing the connection. Formally, using Eqs. (5) and (6), we write:

$$G(A) = \langle RoI(A), E(A) \rangle, \tag{7}$$

where E(A) is the set of edges connecting the RoI nodes.

Figure 2 illustrates the proposed preliminary conceptual model. For an altas $A$ with $n_A = 4$ RoIs, the FSAP graph $G(A)$ is initially structured as a mesh network. For readability, edge weights and labels are omitted. Next, the model demonstrates the characterization of each functional area from the retrieved data and subsequent derivation of the connectome (strictly in relation to $E(A)$).

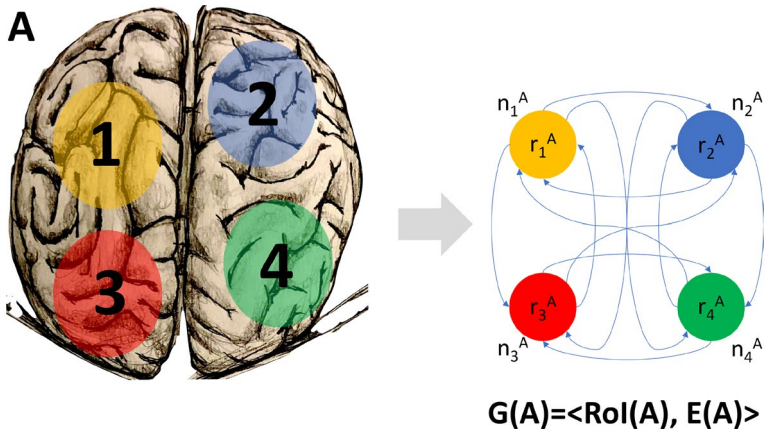


**Fig. 2**. Simplified conceptual example of the FSAP model based on atlas A ($n_A = 4$ RoIs), with the corresponding network graph model defined by Eq. (7) (image generated by PowerPoint from Microsoft 365 Suite, with one hand-made pencil drawing by Maria Mannone).

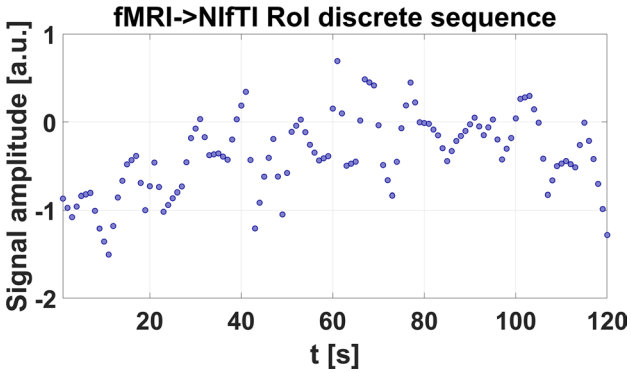


**Fig. 3**. Typical fMRI trend over time (NIfTI), where $T_s = 1$ second and $W_q = 120$, corresponding to the RoI *temporal pole*.

For an individual *k*, the model can be adapted to represent their brain; we therefore rewrite Eq. (7):

$$G_k(A) = \langle RoI_k(A), E_k(A) \rangle, \tag{8}$$

introducing dependence with the specific brain, where $|RoI_k(A)|{=}n_k^A$ and $|E_k(A)|{=}m_k^A$.

For a given brain *k*, the set of nodes *RoI*(*A*) is anatomically defined by atlas *A* and remains unchanged, but the behavior of each agglomerate varies as a function of *k*.

By converting the *DICOM* information into *NIfTI* format, we obtain a discrete, time-dependent sequence of values (i.e., time series) for each RoI. This time series, denoted $TS(r_i^A)_k$, is observed over a time window $W_q$ with sampling period $T_s$. The subscript $q \in \mathcal{N}$ indicates consecutive observation windows (e.g., $W_0 = \{0, 1, 2\}$, $W_1 = \{2, 3, 4\}$, while $|W_q|{=}w$). Expressed formally, we have:

$$\overline{[r_i^A]}_k = \{r_i^A\big|_k(t), t \in W_q\}, \tag{9}$$

where $r_i^A\big|_k(t)$ represents the value of RoI $r_i^A \in RoI_k(A)$ for brain *k*, evaluated at time $t \in W_q$ ($W_q \subset \mathcal{Z}^+$). Thus, for each window $W_q$, the sequence $\overline{[r_i^A]}_k$ is a discrete set of *fMRI* values (in *NIfTI* format) representing the trend in temporal activity of the $i^{th}$ RoI in brain *k* during the observation window. Figure 3 illustrates an example of the trend in activity over time for the RoI corresponding to the *temporal pole*, recorded over observation window $W_q$, with $w = 120$ samples.

## Time series discretization, RoI states and interactions: a deep theoretical analysis

We now model $\overline{[r_i^A]}_k$ as a finite-state discrete process using an approach similar to analog-to-digital (A/D) conversion[54]. As for sampled data from a signal source, the cardinality of the set of possible samples must be reduced, in order to have the chance to assign a finite set of digital words. Given minimum and maximum functional values, we select *M* quantization levels, allowing each $r_i^A$ value to be mapped to a discrete level. To

maintain consistency with the digital resolution, we select $M = 2^n$, where $n$ represents the number of bits of the A/D converter. Although various quantization methods can be applied to perform this operation[55], application of the optimal method for brain data is beyond the scope of the present work. Instead, we employ the mid-tread uniform quantizer[56]. Defining the quantization step as:

$$\Delta_{i,k}^{A} = \frac{1}{M-1} \cdot \left\{ max\{\overline{[r_i^A]}_k\} - min\{\overline{[r_i^A]}_k\} \right\}, \tag{10}$$

the quantization function is subsequently expressed as:

$$Q[r_i^A\big|_k(t)] = \Delta_{i,k}^{A} \cdot \left\lfloor \frac{r_i^A\big|_k(t)}{\Delta_{i,k}^{A}} + \frac{1}{2} \right\rfloor, \tag{11}$$

where the argument is a single time series value. When applied to the full set of values, the quantized time series is denoted $Q[\overline{[r_i^A]}_k]$.

Figure 4 illustrates application of the mid-tread quantizer defined in (11). The red stars denote quantized samples, each assigned to one of the $M = 4$ levels (shown as thick horizontal lines). This indicates that $Q$ is an $M$-valued function: in general, the higher the values of $M$, the lower the quantization-induced distortion and noise in $Q[\overline{[r_i^A]}_k]$.

The final required definition concerns the encoder. Given $M$ and the quantized sequence $Q[\overline{[r_i^A]}_k]$, the corresponding level for each sample is given by:

$$L\left\{Q[r_i^A\big|_k(t)]\right\} = \frac{Q[r_i^A\big|_k(t)] - min\{\overline{[r_i^A]}_k\}}{\Delta_{i,k}^{A}}, \tag{12}$$

where $L : \mathcal{R} \to \mathcal{N}$. The expression in Eq. (12) defines a discrete stochastic process indexed by $t \in W_q$. For a set of $A$, $i$, and $k$, time $t$ is the only independent variable. Therefore, to emphasize its temporal dependence, the quantity on the left side can be written $L\left\{Q[r_i^A\big|_k(t)]\right\}$, in which the initial state is $L\left\{Q[r_i^A\big|_k(0)]\right\}$ and the process evolves over $t \in W_q$. By definition, this process takes values in a discrete state space $S$=[0,...,$M$−1] (assuming a constant $M$ for all atlases $A$, RoI $i$, and brain $k$), and thus is discrete-valued. The quantized time series can now also be modeled using a Markov transition probability matrix (MTPM)[57], which captures the dynamics of each RoI in terms of state transition. Defining the sequence $L\{Q(\overline{[r_i^A]}_k)\}$ as an $M$-state process, the corresponding MTPM (square $M \times M$) over an observation window $W_q$ is defined as:

$$\begin{aligned} MTPM_{i,k}^{A}(\alpha,\beta)\big|_q = & P_q(L\{Q[[r_i^A]_k(\boldsymbol{t_0})]\} = \beta \mid \\ & \mid L\{Q[[r_i^A]_k(\boldsymbol{t_0 - 1})]\} = \alpha), \end{aligned} \tag{13}$$

where $\alpha, \beta \in [0, M-1]$, $t_0 - 1, t_0 \in W_q$, and $P_q$ denotes the conditional probability during $W_q$. Each $MTPM$ element $(\alpha, \beta)$ represents the probability of transitioning from state $\alpha$ to state $\beta$ in consecutive time steps. To be valid, the matrix in (13) must satisfy the condition:

$$\sum_{\beta=0}^{M-1} MTPM_{i,k}^{A}(\alpha,\beta)\big|_q = 1, \tag{14}$$

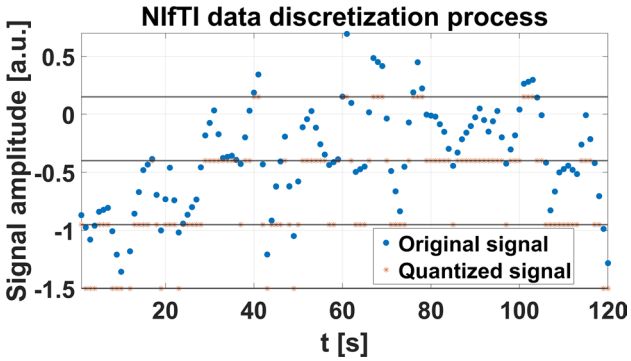


**Fig. 4**. Quantized version of the signal from Fig. 3, with $n = 2$ and $M = 4$. Quantization levels are shown as thick horizontal lines. Discrete time-series values are mapped to the $M$ levels using (11) (red stars), and thus the resulting process assumes only $M$ possible values instead of the original values.

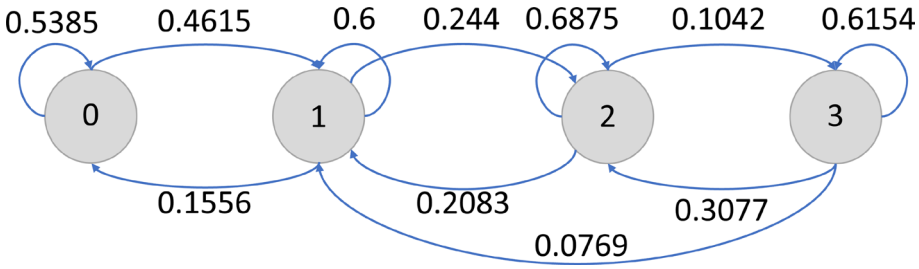


**Fig. 5**. Graphical representation of the FSAP for a single RoI, derived from the quantization in Fig. 4 and the MTPM in (15), with $n = 2$ and $M = 4$.

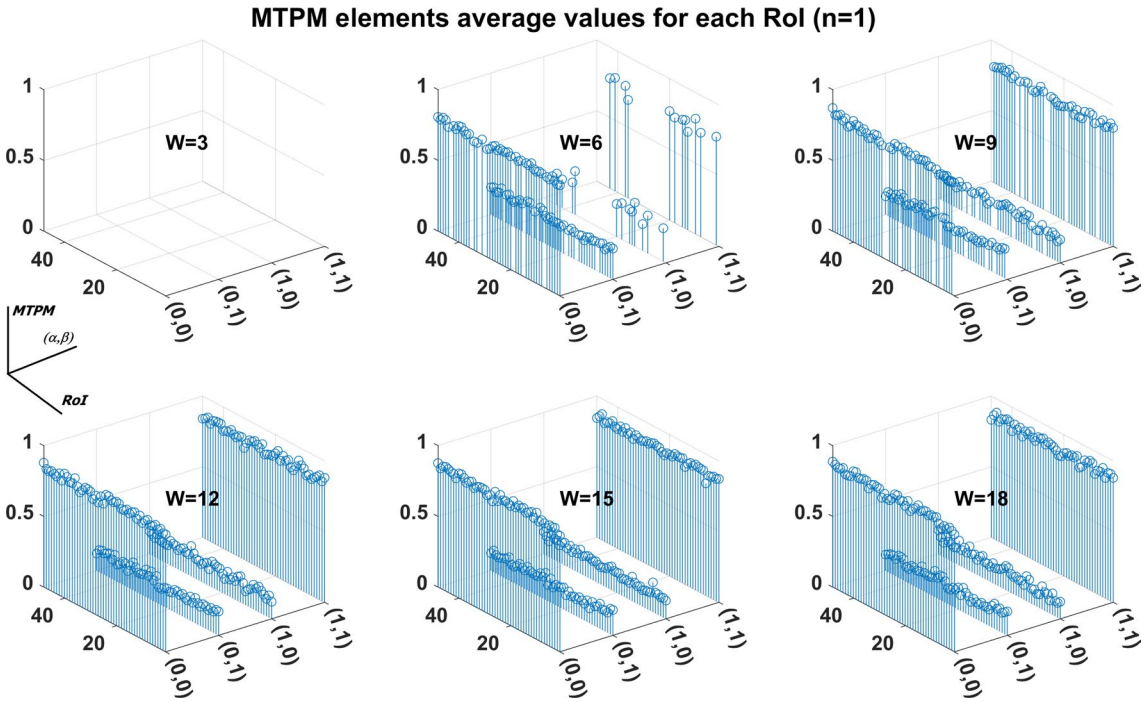


**Fig. 6**. MTPM elements trend for $n = 1$ ($M = 2$) and different values of observation window size *w*.

to ensure that the probability of transitioning from a given state $\alpha$ to another state $\beta$ is 1. For completeness, the FSAP model derived from the examples in Figs. 3 and 4 is presented. In this case, $n = 2$, $M = 4$, and $w = 120$ (i.e., one observation window with $w_0$ samples). The resulting *MTPM* is:

$$MTPM^{A}_{i,k}|_0 = \begin{bmatrix} 0.5385 & 0.4615 & 0 & 0 \\ 0.1556 & 0.60 & 0.244 & 0 \\ 0 & 0.2083 & 0.6875 & 0.1042 \\ 0 & 0.0769 & 0.3077 & 0.6154 \end{bmatrix}, \tag{15}$$

from which it is possible to derive the transition graph for the *i*-th RoI of brain *k* with atlas *A*, shown in Fig. 5.

Before going on with the model extension, it is essential to give an idea of the way *n* and *w* are chosen in our study. From one hand, higher quantization levels brings to a better representation of the process. But, this sentence is true when a huge number of samples is available. In our study, instead, the derived number of NIfTI discrete values is limited (due to both fMRI sampling frequency and patient observation duration). This implies that, if a relatively high number of quantization levels is chosen, the so-called "phantom states" appear: the discretised model will never reach those states during the evolution. A direct consequence of this aspect is the inconsistency of the MTPM matrix because, by definition, it cannot have completely null rows: on the contrary, the sum of each row elements must be 1 (to be defined as markovian matrix).To give a proper idea, Figure 6 has been introduced. In this case, just two states have been considered for quantization ($M = 2$), for different values of $w \in [3, ..., 18]$. From the comparison of the six sub-plots, it is evident that at least $w = 12$ samples are needed for each $q$-th observation, in order to have a complete definition of the MTPM values for each RoI. On the contrary, below that threshold (e.g., $w \in [3, 9]$), it is not possible to completely define the MTPM elements, because some state transitions do not occur for each RoI, leaving undefined values in the model (i.e., inconsistent

MTPM). From Figure 7, it can be seen that the effect is amplified when more statuses are considered: in this case $w = 18$ is still not enough to have a concrete definition of the MTPM($\alpha$, $\beta$) elements. For sake of completeness, also the case of $n = 3$ ($M = 8$) is considered in Figure 8: it is evident how *w* must be much greater than 18 to have an effective and coherent MTPM.

Last but not least, we introduce Figure 9 to show that the best choice for the final model is represented by $n = 2$ and $w = 20$: the MTPM elements are completely and correctly evaluated, $W_q$ are big enough to guarantee the possibility to have several observations for each patient and for the obtained samples after the DICOM to NIfTI conversion. As shown before, the choice of $n = 1$ is also feasible, but this could imply to have only ON-OFF RoIs, without the possibility to account for the *amount* of activity, as will be illustrated later.

The final step to complete the model involves determining which temporal values to generate when the FSAP remains in a given state. From the time series quantization and the properties of the mid-tread quantizer, the exact values corresponding to each quantization level within an observation window $W_q$ can be identified. For each state $s \in S$ of the quantized series $\overline{[r_i^A]}_k = \{r_i^A\big|_k(t)$, we thus define the corresponding values for a mid-tread uniform quantizer:

$$\overline{[r_i^A]}_k^s = \left\{ r_i^A\big|_k(t) \;\middle|\; s \leq \frac{r_i^A\big|_k(t)}{\Delta_{i,k}^A} < s+1, \;\; t \in \bigcup_{q=1}^{w} W_q \right\}. \tag{16}$$

This definition can be adapted to other quantizer types. From the values of $\overline{[r_i^A]}_k^s$ in (16), we compute:

$$\mu_{i,k,s}^A = \mathcal{E}\left[\overline{[r_i^A]}_{k,q}^s\right], \;\; \sigma_{i,k,s}^A = \sqrt{\mathcal{E}\left[\left\{\overline{[r_i^A]}_k^s\right\}^2\right] - \mathcal{E}\left[\overline{[r_i^A]}_k^s\right]^2}. \tag{17}$$

These represent the mean and standard deviation of the values associated with state *s*, independent of the specific observation window $W_q$. Here, $\mathcal{E}$ denotes the expected value. Once the terms of Eqs. (16) and (17) are derived from the empirical process, a statistical realization of the synthetic process can be formulated for the time spent in a particular state $T_s$. Thus:

$$r_{i,k,s}^A(l) = D^*\left(\mu_{i,k,s}^A,\; \sigma_{i,k,s}^A, l\right), \tag{18}$$

where $D$ denotes the selected probability distribution introduced above and numerically characterized in the next section, and $D^*$ denotes a realization of this distribution at a discrete time *l*.

At this stage, each RoI is fully described by the FSAP model, enabling the derivation of several interesting statistics, as demonstrated in the numerical analysis. To complete the example, the values obtained from Eqs. (16) and (17) for the previous case, with $M = 4$, are described below.

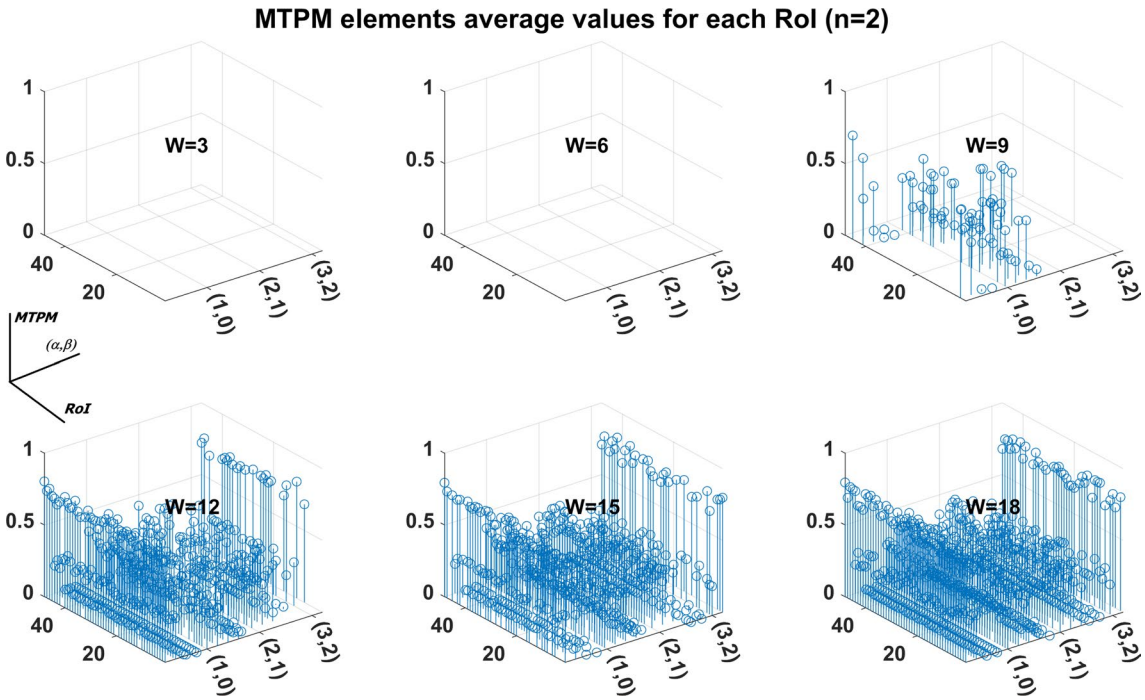


**Fig. 7**. MTPM elements trend for $n = 2$ ($M$=4) and different values of observation window size *w*.

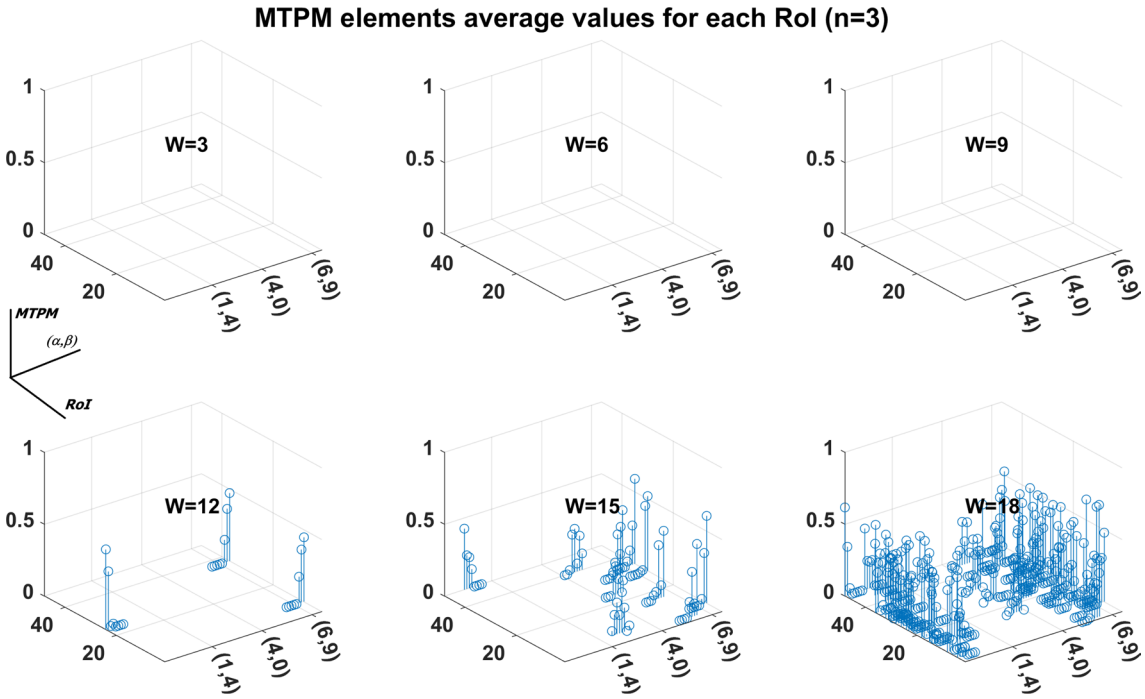


**Fig. 8**. MTPM elements trend for $n = 3$ ($M = 8$) and different values of observation window size $w$.

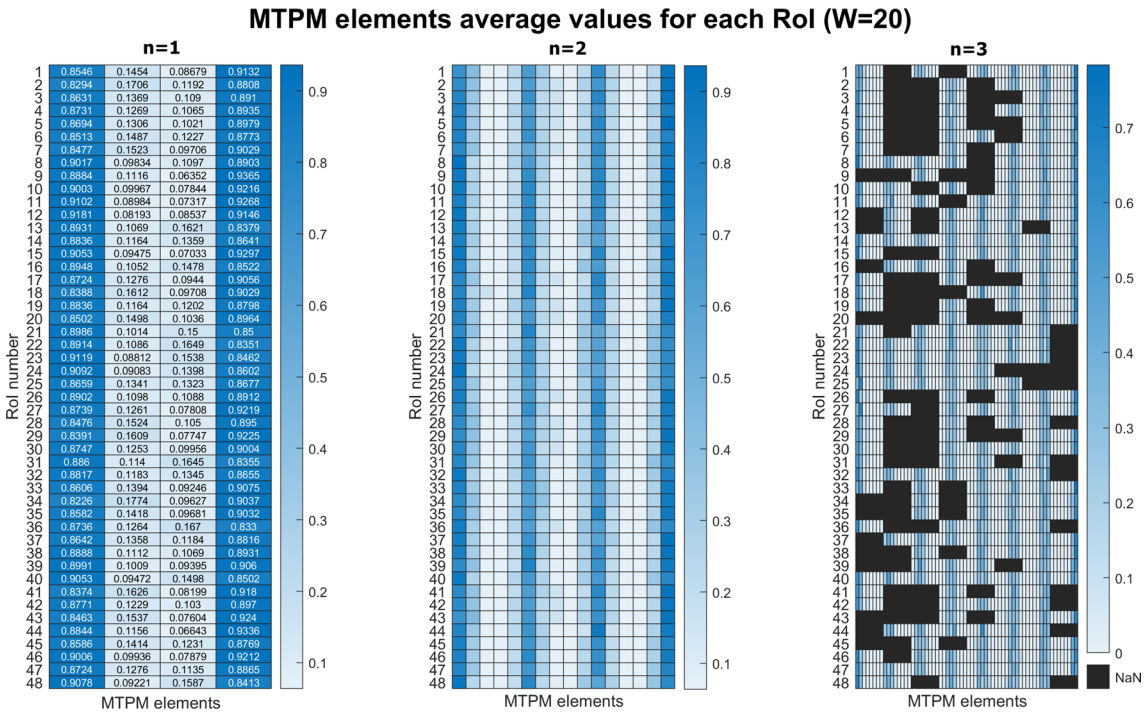


**Fig. 9**. MTPM elements heating maps for $w = 20$ and $n = 1, 2, 3$ ($M$=2,4,8).

Figure 10 shows the original probability density function of the NIfTI value for various bin granularities. The dotted vertical lines correspond to the quantization levels ($S = [0, 1, 2, 3]$, with $s = 0$ aligned to the minimum time series value and $s = 3$ representing the level below the maximum value. The gray regions represent approximation errors resulting from histogram binning; these errors diminish with finer bin resolution.

Using the partition with $M = 4$ (corresponding to the number of bins), we obtain the parameter values summarized in Table 1. For brevity, the tables uses compact notation for parameters previously defined. With this, the element $RoI(A)$ of $G(A)$ is now fully modeled.

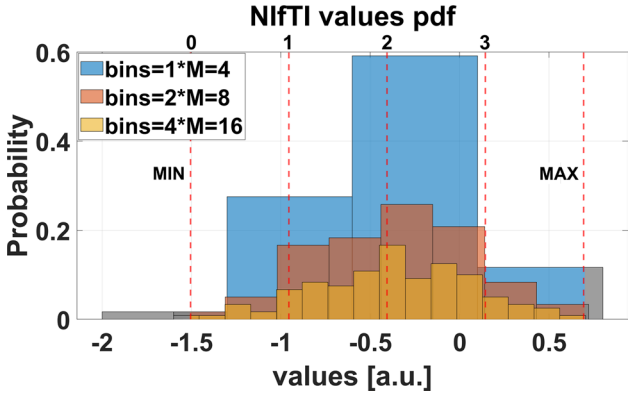


**Fig. 10**. Probability density function of the NIfTI values for various bin granularities, for the samples in Fig. 3.

| M | min | max | $Q_0$ | $Q_1$ | $Q_2$ | $Q_3$ |
|---|---|---|---|---|---|---|
| 4 | −1.504 | 0.693 | −1.504 | −0.955 | −0.406 | 0.144 |
| Δ | $\mu$ | $\sigma$ | $s_0(\mu,\sigma)$ | $s_1(\mu,\sigma)$ | $s_2(\mu,\sigma)$ | $s_3(\mu,\sigma)$ |
| 0.55 | −0.37 | 0.44 | −1.1, 0.13 | −0.6, 0.17 | −0.14, 0.14 | 0.33, 0.15 |

**Table 1**. FSAP parameters for the example in Fig. 3.

To determine $E_k(A)$, the relationships between RoIs must now be established. A deeper analysis of the distributions and associated values is presented in the next section. As a starting point, we applied the Spearman correlation (SC) for time series analysis[58,59]. SC is based on the concept of ranking, which fits perfectly with our modeling proposal, given the NIfTI data discretization process illustrated before. Returning to Eqs. (8) and (9), the edges of the graphs, specifically their weights, can be defined for each pair of RoIs. For the quantized time series $[r_m^A]_k$ and $[r_n^A]_k$, the SC between the two RoIs in $W_q$ for individual $k$ is given by[59], deriving it from Pearson's correlation (PC)[58]:

$$
\begin{aligned}
PC_{k,q,s}(m,n) &= \frac{\sum_{l\in W_q}[r^A_{m,k,s}(l)-\mu^A_{m,k,s}]\cdot[r^A_{n,k,s}(l)-\mu^A_{n,k,s}]}{\sqrt{\sum_{l\in W_q}[r^A_{m,k,s}(l)-\mu^A_{m,k,s}]^2\cdot\sum_{l\in W_q}[r^A_{n,k,s}(l)-\mu^A_{n,k,s}]^2}},\\
SC_{k,q,s}(m,n) &= \frac{\sum_{l\in W_q}[Q(r^A_{m,k,s}(l))-Q(\mu^A_{m,k,s})]\cdot[Q(r^A_{n,k,s}(l))-Q(\mu^A_{n,k,s})]}{\sqrt{\sum_{l\in W_q}[Q(r^A_{m,k,s}(l))-Q(\mu^A_{m,k,s})]^2\cdot\sum_{l\in W_q}[Q(r^A_{n,k,s}(l))-Q(\mu^A_{n,k,s})]^2}}\\
&= 1-\frac{6\cdot\sum_{l\in W_q}[Q(r^A_{m,k,s}(l))-Q(r^A_{n,k,s}(l))]^2}{w\cdot(w^2-1)},
\end{aligned}
\tag{19}
$$

where Q( ) represents the quantized value of ( ), as introduced in eq. (11).

Figure 11 shows an example of the correlation tests that have been carried out for the complete set of RoIs: for sake of readability we show only the first 8 RoIs for patient $k = 1$. In addition, from Figure 12 it is evident that the Spearman's hypothesis is valid, because most of the p-vales are negligible. From Eq. (19), it is clear that $SC_{k,q,s}(m,n)$ assumes values in the range [−1, 1] (the sign is determined by multiplication at the numerator), and $SC_{k,q,s}(m,n)$=$SC_{k,q,s}(n,m)$.

After a careful analysis of the obtained data, we can say that Spearman's correlation test is better than BC (the assumption of a linear dependence between the observed variables is removed); however, also SC have several limitations for our model, especially: (1) the output range is not normalized to the range [0,1]; (2) a monotonic dependence between each pair of RoIs is assumed; (3) symmetric values are produced on account of the numerator's commutative property. Positive and negative correlation values indicate a similar trend in the variables. Typically, a positive correlation suggests that as one variable increases, the other also increases, and vice-versa. In the context of brain parcellation, however, negative and positive *NIfTI* values convey equivalent information, such as specific stimuli (e.g., moving forward or backward)[60,61]. One possible solution is to rescale *NIfTI* values to the positive real domain $\mathcal{R}_0^+$, but the dynamic nature of the time window $W_q$ prevents the identification of a global minimum across all temporal ranges. Therefore, we apply an alternative metric to overcome BC's and SC's limitations. Unlike previously applied approaches, we incorporate mutual information (MI) and normalized mutual information (NMI). An information theory concept, MI quantifies the amount of information about one random variable obtained through another random variable (i.e., it reflects the reduction in uncertainty about one variable given knowledge of the other). Studies have shown that MI has greater accuracy

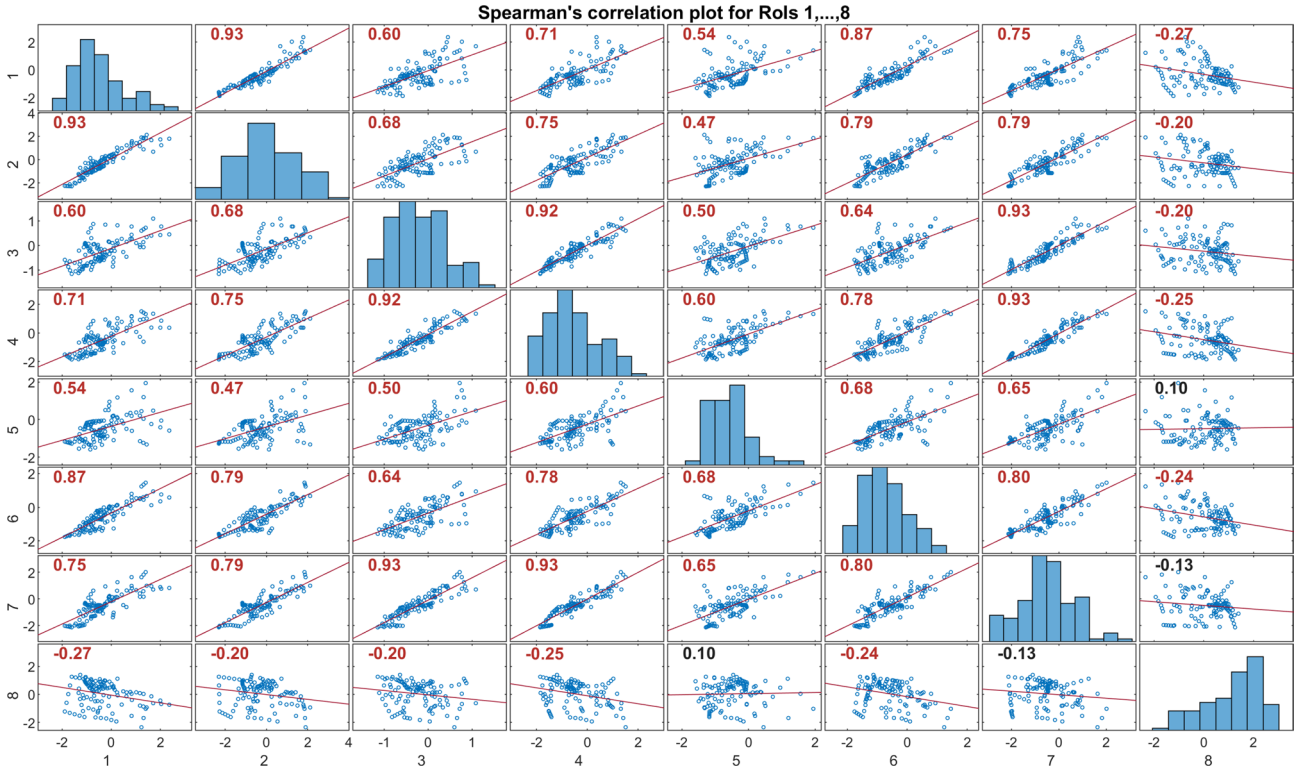


**Fig. 11**. Example of Spearman correlation test, for $k = 1$, RoI$= 1, \ldots, 8$, $w = 120$: SC is evaluated for each couple of RoI.

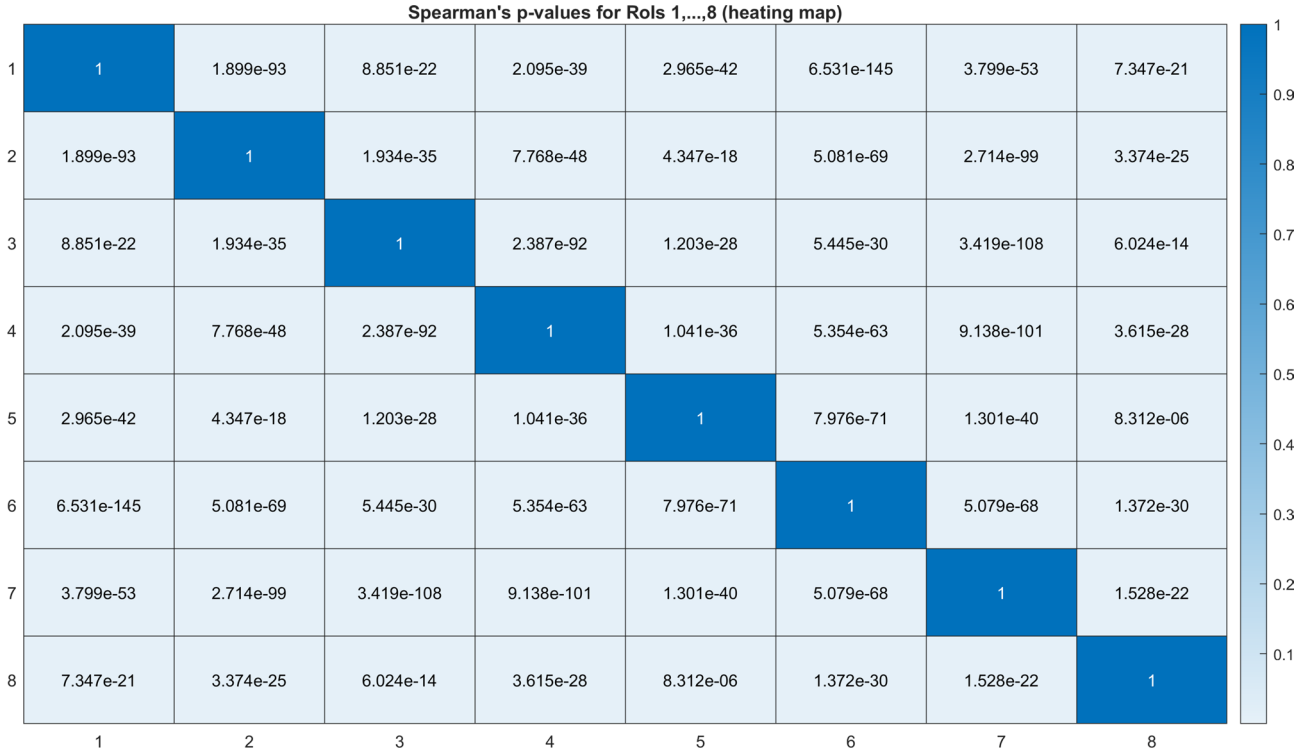


**Fig. 12**. Spearman correlation test p-values, for $k = 1$, RoI$= 1, \ldots, 8$, $w = 120$: SC is evaluated for each couple of RoI.

than SC and BC with certain diseases, since it does not rely on the assumption of neither linear dependence nor monotonic relation between RoIs[62,63]. For completeness, MI is defined as:

$$\begin{aligned} MI^{A}_{k,q,s}(m,n) = \\ = \sum_{l_1 \in W_q} \sum_{l_2 \in W_q} P_{m,n}\left[r^{A}_{m,k,s}(l_1), r^{A}_{n,k,s}(l_2)\right] \cdot \\ \cdot log\left\{\frac{P_{m,n}\left[r^{A}_{m,k,s}(l_1), (r^{A}_{n,k,s}(l_2))\right]}{P_m\left[r^{A}_{m,k,s}(l_1)\right] \cdot P_n\left[r^{A}_{n,k,s}(l_2)\right]}\right\}, \end{aligned} \tag{20}$$

where $P_{m,n}$ is the joint probability function of $r^{A}_{m,k,s}$ and $r^{A}_{n,k,s}$, and $P_m$ and $P_n$ are the corresponding marginal probability distributions. In the absence of any mutual correlation between RoI *m* and RoI *n*, the term $P_{m,n}\left[r^{A}_{m,k,s}(l_1), r^{A}_{n,k,s}(l_2)\right]$ becomes negligible and $MI^{A}_{k,q,s}(m,n)$ reduces to zero, consistent with the limit:

$$\lim_{x \to 0} x \cdot log(x) = 0. \tag{21}$$

The final step involves normalizing the MI between 0 and 1 to obtain the NMI[64]:

$$NMI^{A}_{k,q,s}(m,n) = \frac{2 \cdot MI_{k,q,s}(m,n)}{H(r^{A}_{m,k,s}) + H(r^{A}_{n,k,s})}, \tag{22}$$

where $H(\cdot)$ denotes the entropy function. Fig. 13 presents the resulting MI and NMI values for the dataset applied in Fig. 11.

This formulation captures the relationship between two RoIs as a function of time and defines the term $E_k(A)$, which falls in the range [0,1], has no mandatory linear dependence, and is not always symmetric. The next section describes the derivation of a real network from $G_k(A)$.

## From brain activity to networking

Using the elements of $G_k(A)$ (Eq. (8) and Fig. 2), we outline the derivation of a networking model.

A set of FSAPs (e.g., a brain, as illustrated in Fig. 2) can be modeled as a STATic Ad-hoc NETwork (STATNET) in which node mobility is zero (i.e., node position in the geographical deployment area remains fixed). In contrast, node availability and connections vary over time. The network is updated at regular intervals of $T_s$. Each node in $RoI_k(A)$ follows the FSAP model (Section "Time Series Discretization, RoI States and Interactions: a deep theoretical analysis"). Once its statistical properties are derived (Eq. (18)), a node's transmission/reception activity can be defined. Since negative and positive *NIfTI* RoI values carry equal informational weight, the conditions under which a node operates in receiving (RX), transmitting (TX), or combined (TX/RX) state must be defined. To associate the appropriate FSAP state with each RoI, previous studies[60,61] suggest assigning the resting state (RX) to the lowest NIfTI values. This assumes that no data are generated by any RoI when its value is discretized to state 0. Accordingly, the *i*-th RoI is considered to be transmitting data if and only if:

$$L\{Q[r^{A}_{i}|_k(\boldsymbol{t})]\} \neq 0. \tag{23}$$

Here, all node connections are full-duplex, permitting simultaneous transmission and reception over the same link. Equation (23) defines the *TX/RXstate*. Fig. 14 summarizes the concepts discussed, comparing an RoI to a network node.

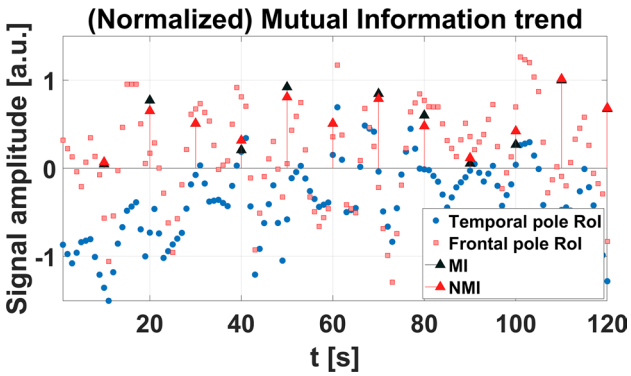


**Fig. 13**. Example of MI and NMI values: the black and red markers indicate MI and NMI, respectively, for the samples applied in Fig. 11 for $w = 10$.

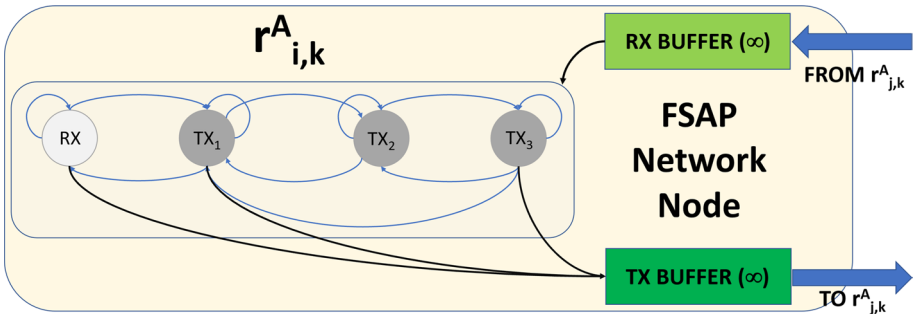


**Fig. 14**. TX/RX and RX states in the FSAP model of Fig. 5. The light color state ($s_0$) denotes the *RX* state, while $s_1, s_2, s_3$ correspond to the TX/RX state. The FSAP model is compared to a static network node capable of transmitting and receiving data via $E_k(A)$ connections to other RoIs, with infinite buffer capacity.

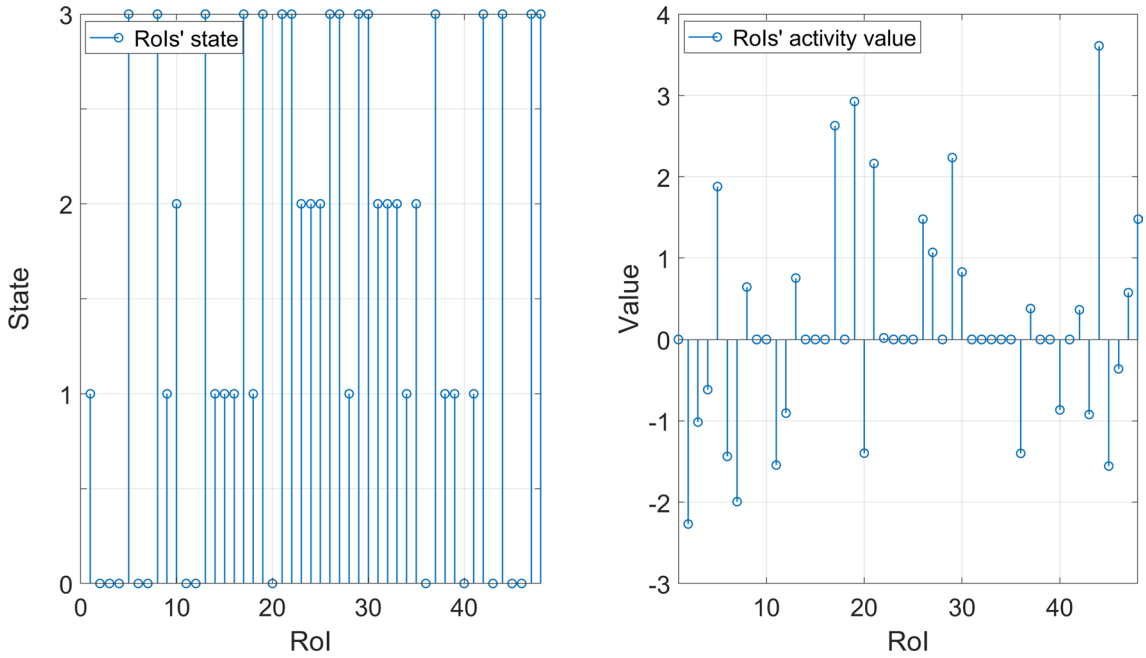


**Fig. 15**. Example of a time snapshot of RoI evolution for $M = 4$. Left: the $M$ possible states $L\{Q([\overline{r_i^A}]_k])\}$ distributed across 48 RoIs. Right: the corresponding realizations $r^A_{i,k,s}$ assumed by each RoI.

As shown in Fig. 14, each node consists of an internal core network responsible for determining its current state, hence its activity level $L\{Q([\overline{r_i^A}]_k])\}$) and TX/RX interfaces (which correspond to synaptic connections between RoIs) are shown in Fig. 15.

Regarding data transmission, each RoI is assumed to generate traffic according to a variable Poisson packet rate (VPPR) model[65]. For each of the $M-1$ states (state 0 considered the RX state), different levels of Poisson traffic are produced[66], with rates proportional to $r^A_{i,k,s}$, Eq. (18).

To visually represent the STATNET model derived from the above formulation, Fig. 16 presents an example of the $G_k(A) = \langle RoI_k(A), E_k(A)\rangle$ topology. On the left, the matrix of $NMI_{k,q,s}(m,n)$ values is shown as a heat map, and the corresponding graphical representation of $G_k(A) = \langle RoI_k(A), E_k(A)\rangle$ appears on the right.

For a generic window $W_q$, each RoI $i$ evolves over a time interval of $w \cdot T_s$, assuming values $r^A_{i,k,s}(l)$ for $l \in W_q$. When $L\{Q[r^A_{i,k,s}(l)]\} \neq 0$ (indicating a TX state), each RoI generates traffic proportional to $|r^A_{i,k,s}(l)|$ [60,61]. The quantity of generated data is denoted $D^A_{i,k,s}(l)$, under the condition established in Eq. (23). Assuming that packet generation follows a Poisson distribution, we write:

$$T^A_{i,k,s}(l) = -\frac{ln(rand_u)}{|r^A_{i,k,s}(l)| \cdot K_m}, \tag{24}$$

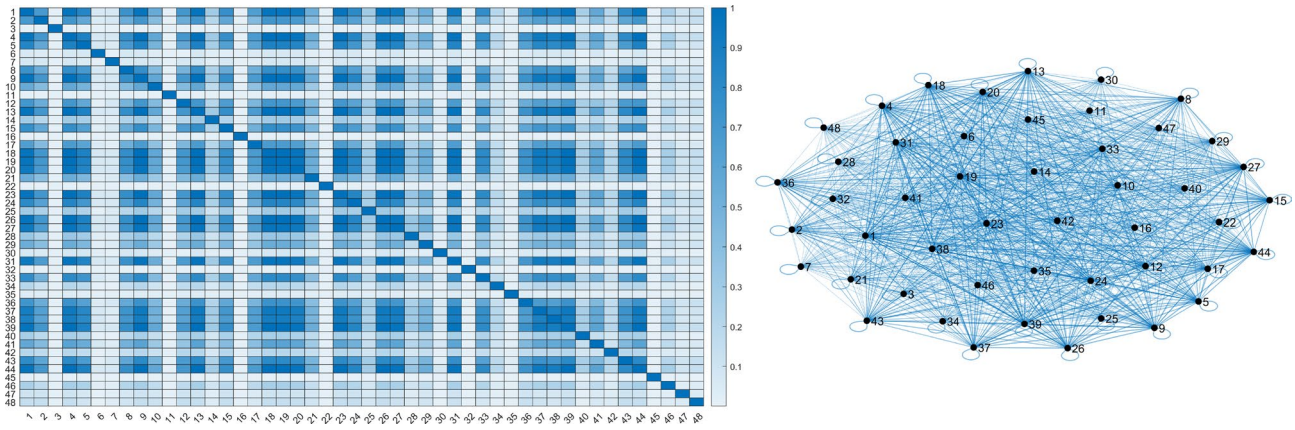

**Fig. 16**. Example of $NMI_{k,q,s}(m,n)$ values represented as a heat map (left) and corresponding graph (right), with edge thickness proportional to the *NMI* weights; $w = 20$.

where $rand_u$ is a uniformly distributed number in the interval (0,1), and $T^A_{i,k,s}(l)$ is the packet inter-arrival time during the *l*-th observation of individual *k* under atlas *A* for the *i*-th RoI, which remains in state *s*. The constant term $K_m$ [Hz] is evaluated as follows:

$$K_m = \frac{EN_m \cdot 9.8}{P_{size} \cdot 8} \cong 1.225 \cdot \frac{EN_m}{P_{size}}, \tag{25}$$

where $EN_m$[67–72] is the average number of Estimated Neurons for RoI *m* (illustrated in Table 2 for a human brain of adult patients, 60–80 years old), 9.8 [bps] is the typical neuronal bit generation rate and $P_{size}[B]$ is the packet size (typically set to 1500, as the Maximum Transmission Unit, MTU, of IP networks). Larger absolute values of $r^A_{i,k,s}(l)$ indicate a higher packet generation rate.

It is important to clarify the distribution of generated traffic to other RoIs: specifically, how the NMI (Eq. (22)) guides the forwarding of packets to existing links according to their weights. In the context of a telecommunications system, we refer to the meaning of NMI and $E_k(A)$ in STATNET as the system's *metric*. In particular, we take into account the *Brain Activity* concept, for which data is transmitted over active links in proportion to their dynamic weights, defined as:

$$D^A_{k,q,s}(m,n) = w \cdot T_s \cdot \frac{NMI_{k,q,s}(m,n)}{\sum\limits_{n|_{NMI_{k,q,s}(m,n)>0}} NMI_{k,q,s(m,n)}} \cdot \sum_{l \in W_q} \frac{1}{T^A_{m,k,s}(l)}. \tag{26}$$

Here, a link from node *m* to node *n* is considered active when $NMI_{k,q,s}(m,n) > 0$, with $w \cdot T_s$ is the duration (in seconds) of window $W_q$; the final summation expresses the packet rate in Hz (1/s), as in eq. (24).

While many other metrics can be defined for a telecommunications network[73], the presented analysis focuses solely on the metric outlined above.

## Experimental evaluation: cases of individuals with healthy and diseased brains

This section presents an evaluation of the proposed telecommunication-inspired model applied to cases of individuals with healthy and diseased brains.

### General assessment

We begin by highlighting that the ADNI (ADNI 2) dataset applied in this study comprises data compiled from both healthy individuals and patients diagnosed with AD. As regards the considered patients, Figure 17 shows the way the selected data has been considered and clustered, in order to have the possibility to compare the obtained results: a total of 27 patients has been analyzed, with $k = 1, \ldots, 27$, grouped in two main sets over 70 (age $\geq$ 70 years) and under 70 (age < 70 years). We focus on selected patients, representative of a restricted age range, where age effects starts playing a role also for healthy subjects. All details have been implemented in MATLAB and the full code is available at https://github.com/medusamedusa/fMRI_telecommunications.

The model was configured according to the Harvard-Oxford atlas, and the RoIs set was defined as $RoI_k(A) = \{r^A_1, \ldots, r^A_{48}\}$, thus with $n^A_k = 48 = n^A$, independently of the individual *k*. The sampling interval $T_s$ was set to 0.25 seconds, as determined by the dataset, corresponding to a frequency of $f_s = 4$ Hz. Fig. 18 shows the typical numerical trend of the NIfTI file content for the first healthy control ($k = 1$). These data are the initial input to the model. For completeness, the available data was parceled and grouped into five anatomical lobes (Frontal lobe, Lobo-temporal lobe, Parietal lobe, Occipital lobe and Limbic lobe).

The primary aim of this work is to investigate the intrinsic trend dynamics of each RoI and lobe by modeling them as a static network. This framework permits meaningful distinctions between healthy and diseased brain

| RoI # | Name | Approx. Volume ($mm^3$) | ENs ($\cdot 10^9$) | $K_m$ (Hz) |
|---|---|---|---|---|
| 1 | Frontal Pole | 18000 | 0.465658 | 380.287 |
| 2 | Insular Cortex | 11500 | 0.297348 | 242.834 |
| 3 | Superior Frontal Gyrus | 22000 | 0.566644 | 462.759 |
| 4 | Middle Frontal Gyrus | 21000 | 0.541397 | 442.141 |
| 5 | Inferior Frontal Gyrus, pars triangularis | 14500 | 0.373087 | 304.688 |
| 6 | Inferior Frontal Gyrus, pars opercularis | 13800 | 0.356256 | 290.943 |
| 7 | Precentral Gyrus | 18500 | 0.476879 | 389.451 |
| 8 | Temporal Pole | 10000 | 0.258075 | 210.762 |
| 9 | Superior Temporal Gyrus, anterior division | 15500 | 0.401139 | 327.597 |
| 10 | Superior Temporal Gyrus, posterior division | 14800 | 0.381503 | 311.561 |
| 11 | Middle Temporal Gyrus, anterior division | 17000 | 0.437606 | 357.378 |
| 12 | Middle Temporal Gyrus, posterior division | 16500 | 0.425682 | 347.635 |
| 13 | Inferior Temporal Gyrus, anterior division | 16000 | 0.413759 | 337.891 |
| 14 | Inferior Temporal Gyrus, posterior division | 15800 | 0.408797 | 333.838 |
| 15 | Postcentral Gyrus | 19000 | 0.489803 | 400.014 |
| 16 | Superior Parietal Lobule | 17500 | 0.451727 | 368.524 |
| 17 | Supramarginal Gyrus, anterior division | 16200 | 0.418720 | 341.943 |
| 18 | Supramarginal Gyrus, posterior division | 15900 | 0.410990 | 335.683 |
| 19 | Angular Gyrus | 16800 | 0.433644 | 354.402 |
| 20 | Lateral Occipital Cortex, superior division | 15000 | 0.387463 | 316.430 |
| 21 | Lateral Occipital Cortex, inferior division | 14800 | 0.381503 | 311.561 |
| 22 | Intracalcarine Cortex | 9000 | 0.232829 | 190.144 |
| 23 | Cuneal Cortex | 8800 | 0.227867 | 186.092 |
| 24 | Lingual Gyrus | 13500 | 0.348333 | 284.070 |
| 25 | Superior Occipital Gyrus | 14000 | 0.361217 | 294.844 |
| 26 | Middle Occipital Gyrus | 14500 | 0.373087 | 304.688 |
| 27 | Inferior Occipital Gyrus | 13800 | 0.356256 | 290.943 |
| 28 | Parahippocampal Gyrus, anterior division | 12000 | 0.309217 | 252.527 |
| 29 | Parahippocampal Gyrus, posterior division | 11800 | 0.304256 | 248.474 |
| 30 | Hippocampus | 6000 | 0.154845 | 126.263 |
| 31 | Amygdala | 3500 | 0.090327 | 73.654 |
| 32 | Thalamus | 7200 | 0.185616 | 151.000 |
| 33 | Caudate | 6800 | 0.175693 | 143.126 |
| 34 | Putamen | 7000 | 0.180655 | 147.179 |
| 35 | Pallidum | 4500 | 0.116134 | 94.790 |
| 36 | Accumbens | 1800 | 0.046586 | 38.029 |
| 37 | Temporal Fusiform Cortex, anterior division | 12500 | 0.322594 | 263.452 |
| 38 | Temporal Fusiform Cortex, posterior division | 13000 | 0.336620 | 274.906 |
| 39 | Temporal Occipital Fusiform Cortex | 12800 | 0.331010 | 270.325 |
| 40 | Occipital Fusiform Gyrus | 12200 | 0.314179 | 256.579 |
| 41 | Frontal Opercular Cortex | 10800 | 0.277712 | 226.798 |
| 42 | Central Opercular Cortex | 10200 | 0.263686 | 215.343 |
| 43 | Parietal Opercular Cortex | 9800 | 0.252465 | 206.180 |
| 44 | Planum Polare | 8500 | 0.218803 | 178.689 |
| 45 | Heschl's Gyrus | 8200 | 0.210388 | 171.817 |
| 46 | Planum Temporale | 10500 | 0.272101 | 222.216 |
| 47 | Supracalcarine Cortex | 8000 | 0.207582 | 169.526 |
| 48 | Occipital Pole | 9500 | 0.244050 | 199.307 |

**Table 2**. RoI volumes, estimated number of neurons (ENs), and $K_m$ values for the nodes of the STATNET model.

states. Although the dataset comprises discrete values, they are plotted as continuous curves to deepen visual readability.

At this analysis stage, the available data were quantized by selecting a quantization level $M$, which also defines the number of states in each RoI's FSAP model, as introduced in Eqs. (10) to (13). As discussed in the previous section, in the simulations we set $M = 4$ ($n = 2$) and the observation window size $w = 20$. Using

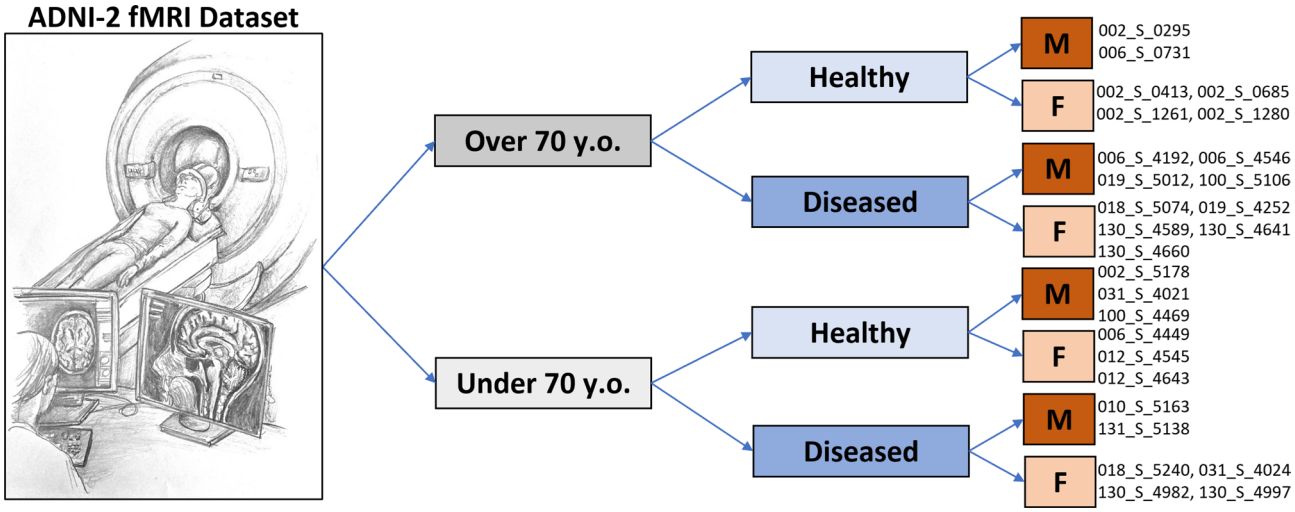


**Fig. 17**. A conceptual representation of the ADNI 2 dataset clustering; considered patients ADNI IDs are written on the right side (image created via PowerPoint from Microsoft 365 Suite, with one hand-made pencil drawing by Maria Mannone).

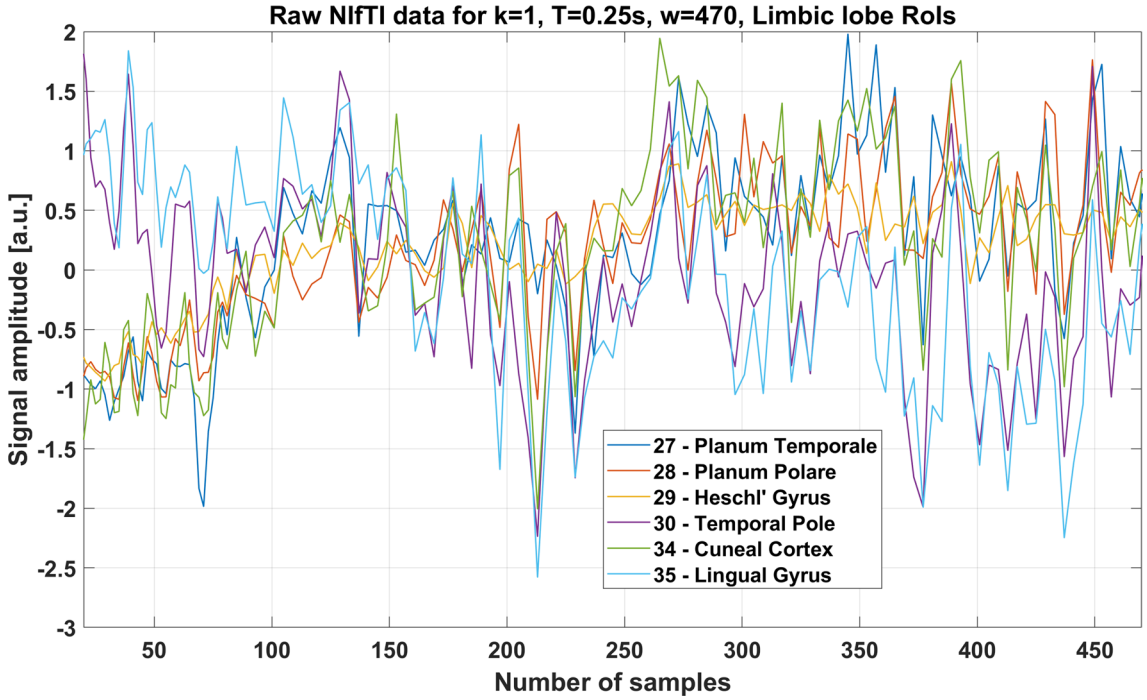


**Fig. 18**. An example of real signal trends from the NIfTI file for $A$='Oxford-Harvard', $n_k^A = 48$ RoIs, and Limbic lobe RoIs (27, 28, 29, 30, 34, 35), shown as distinct colored curves (healthy male patient, 90 years old, ADNI id: 002 S 0295).

these parameters, we computed the MTPM over time and examined the temporal evolution of selected matrix elements. Focusing on the first three observation windows ($q = 0, 1, 2, 3$), we determined the complete MTPMs for $k = 2$ (over 70, healthy control). Concrete examples are shown in equations (27), (28):

$$MTPM^A_{0,2|0} = \begin{bmatrix} 0.71428 & 0.28572 & 0 & 0 \\ 0.22222 & 0.66667 & 0.11111 & 0 \\ 0 & 1 & 0 & 00 \\ 0 & 0 & 0.50000 & 0.50000 \end{bmatrix} MTPM^A_{0,2|1} = \begin{bmatrix} 0.50000 & 0.50000 & 0 & 0 \\ 0.50000 & 0 & 0.50000 & 0 \\ 0 & 0.10000 & 0.6000 & 0.30000 \\ 0 & 0 & 0.3333 & 0.6667 \end{bmatrix} \quad (27)$$

$$MTPM^A_{0,2}|_2 = \begin{bmatrix} 0.60000 & 0.40000 & 0 & 0 \\ 0.60000 & 0 & 0.20000 & 0.20000 \\ 0 & 0.40000 & 0.40000 & 0.20000 \\ 0 & 0.20000 & 0.40000 & 0.40000 \end{bmatrix} MTPM^A_{0,2}|_3 = \begin{bmatrix} 0.6750 & 0.32500 & 0 & 0 \\ 0.50000 & 0 & 0.25000 & 0.25000 \\ 0 & 0.30000 & 0.40000 & 0.30000 \\ 0 & 0.10000 & 0.30000 & 0.60000 \end{bmatrix} \quad (28)$$

Fig. 19 illustrates the trend of $MTPM^A_{1,k}(0,0)\big|_q$ over 23 observation windows for RoI $i = 1$ (frontal pole), with parameters $w = 20$ and $M = 4$. The first three values in the graph exactly match those reported by Eqs. (27) and (28) for $(\alpha, \beta) = (0, 0)$.

A more detailed example is given in Fig. 20, which shows the trend of $MTPM^A_{17,k}(0,0)\big|_q$ for four cases: $k = 1$, $k = 2$, $k = 15$ (healthy control), and $k = 7$ (individual with AD).

The main aim of the proposed model, more detailed in the next sub-section, is to distinguish between healthy and diseased RoIs, identify affected brain regions, and evaluate the average performance in both healthy and diseased brains. Until now, analysis has focused on individual RoI behaviors; the proposed model, however, also incorporates the communication between RoIs. Before the discussion of the distributed parameters (related to $E_k(A)$), a summarizing visualization is presented: Fig. 21 shows a sample distribution of the MTMP(0,0) element across Occipital lobe RoIs for $k = 1$.

Figure 22 offers a view of the NMI metric, illustrating an example of the interactions between RoIs during the observation window $W_q$ ($q = 140$ in this case).

## Specific analysis and STATNET characterization

For the STATNET model, the topology is always the same, independently from *k*. Thus $G_k(A) = \langle RoI_k(A), E_k(A)\rangle$, $n^A_k = 48$, $m^A_k = n^A_k \cdot (n^A_k - 1)/2 + n^A_k = 1776$, considering the mesh topology and the elements (i,i) of $E_k(A)$, $n = 2$ ($M = 4$) and $w = 20$. The topology corresponds to that depicted in Fig. 23 on the left side, while a sample magnification is shown on the right side, to give a better idea of how a mesh topology has been considered. Previous studies have focused on such representations yet overlooked the temporal dynamics of data transmission. Figure 23 shows a still image of the STATNET links, while the code available in https://github.com/medusamedusa/fMRI_telecommunications gives the opportunity to see how the intensity of the links varies over time, in relation to the NMI.

As introduced in sub-section "From Brain Activity to Networking", according to recent studies on neuronal and synaptic capacity[67,69,70,74–76], a single neuron generates information at approximately 10 bps, a synapse stores and transfers around 4.7 bits, and the estimated number of neurons is approximately 86 billions (with the 18.5% distributed in the cortical area). Based on these estimates, on Table 2 and on equations (24), (25), (26), a minimum packet inter-arrival time of 0.5ms is obtained, which corresponds to variable full-duplex links with a maximum bit-rate of 24Tbps (for the Superior Frontal Gyrus RoI). Hence, the possible throughput value between each couple of RoIs belongs to the range [0, 24] Tbps. The simulation duration is set to 500 seconds.

Figure 24 illustrates the trend (in the form of heating-map) of the average total number of packets exchanged in the STATNET topology. Each matrix element (*m*, *n*) represents the relative intensity of packet transmission

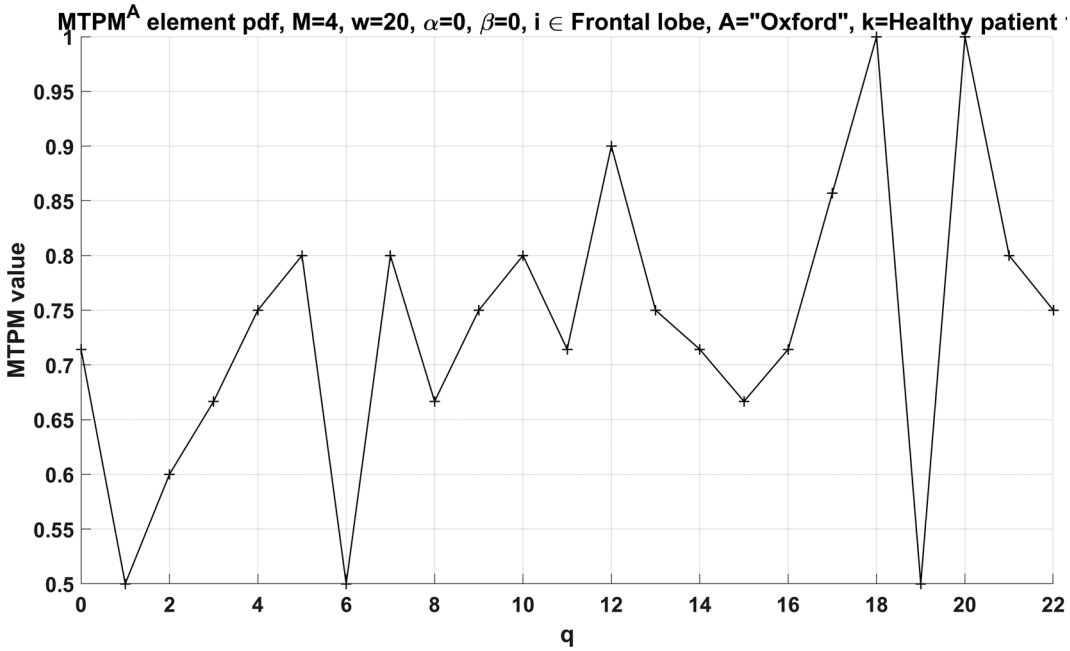


**Fig. 19**. Trend of $MTPM^A_{1,k}(0,0)\big|_q$ over 23 observation windows for RoI $i = 1$ (frontal pole), $w = 20$ and $M = 4$.

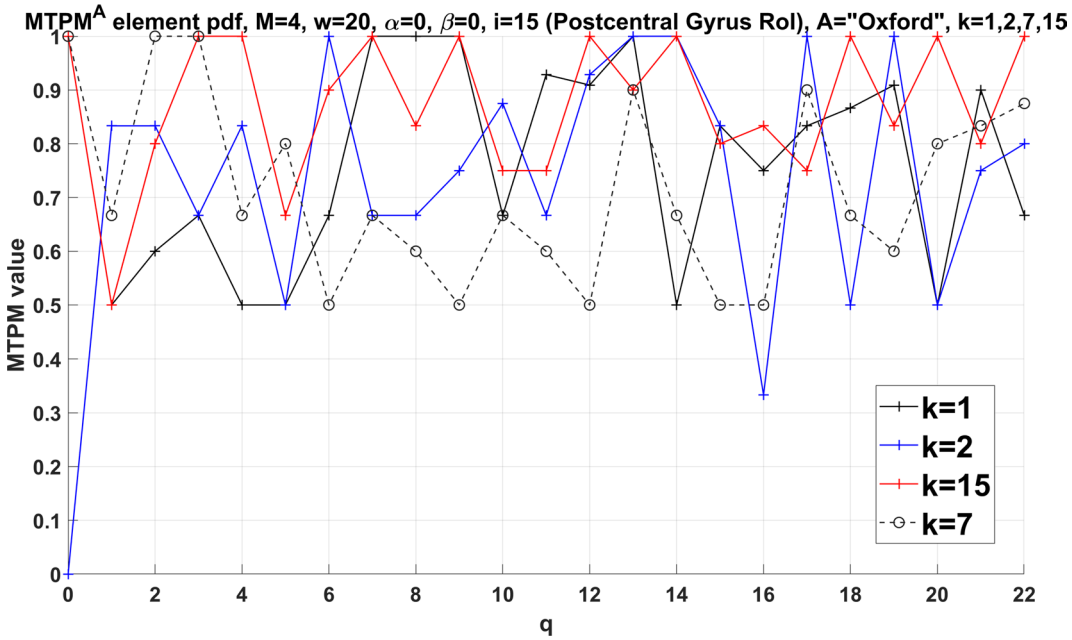


**Fig. 20**. Trend of $MTPM^{A}_{17,k}(0,0)\big|_{q}$ over 23 observations for $i = 15$ (Postcentral Gyrus RoI), with parameters $w = 20$ and $M = 4$, for individuals $k = 1, 2, 15, 7$.

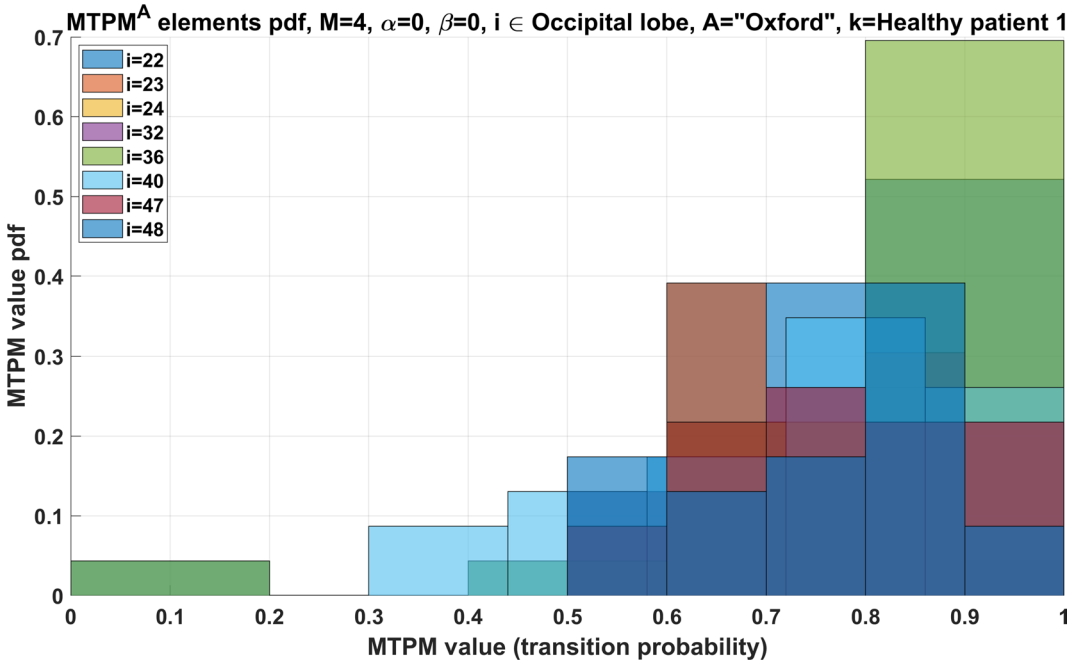


**Fig. 21**. Distribution of the (0,0) MTPM elements across the frontal lobe RoIs for healthy individual $k = 1$.

from RoI $m$ to RoI $n$, including intra-RoI activity for $m$ (i.e., elements $(m, m)$). The ADNI datasets illustrated in Fig. 17 have been grouped as a binary tree, such as the configuration 000 refers to over-70, healthy, males, the configuration 001 refers to over-70, healthy, females, the configuration 010 refers to over-70, diseased, males, and so on. The heating-maps have been obtained as the averages over the number of patients included in each leaf. Fig. 24 shows that, independently from the sex and the age, the number of transmitted packets for diseased patients is much lower than the ones for healthy case.

To provide a preliminary comparison, Fig. 25 presents the pdf of the mean total transmitted packets (MTTP) per RoI for the clustered individuals (also in this case, results have been averaged for each class). It is clear that the means are different and much lower for the diseased case, confirming the lower network activity.

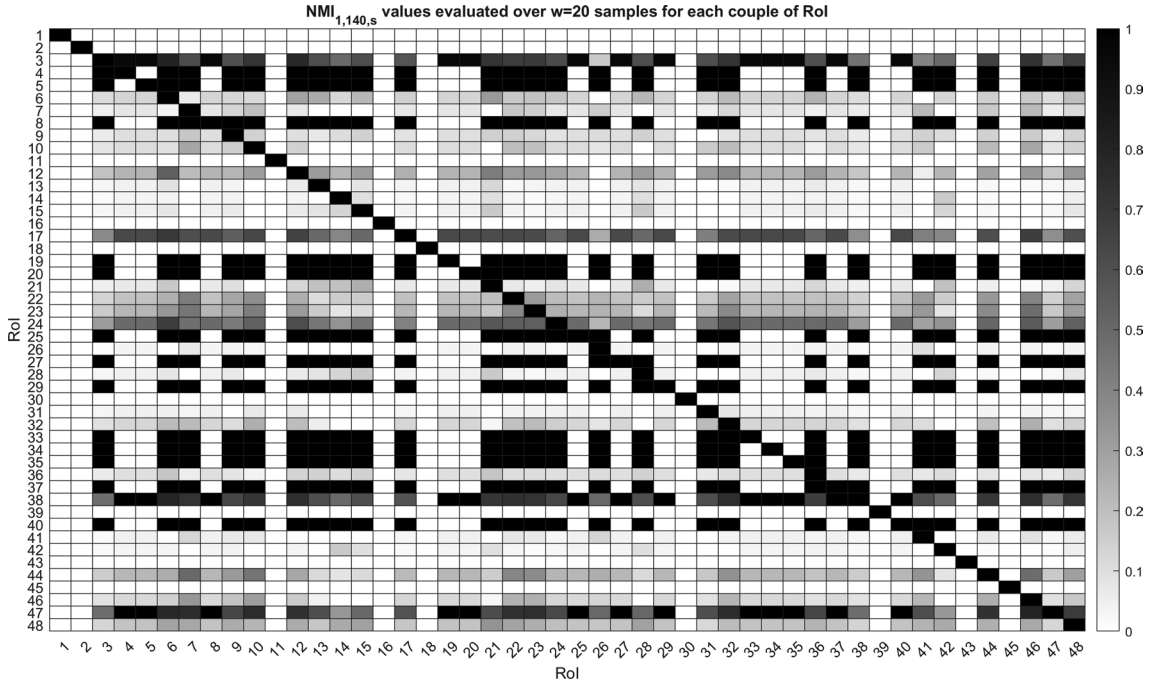


**Fig. 22**. Example of $NMI^{A}_{k,q,s}$ (as defined in Eq. (22)) for $k = 1$, $q = 140$, $s \in [0, ..., 3]$ and $t \in W_{140}$.

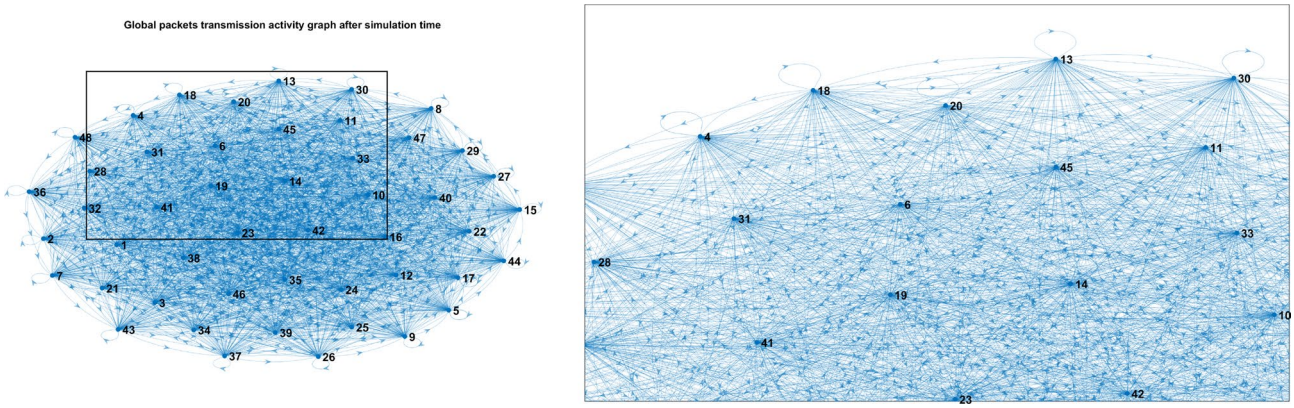


**Fig. 23**. Simulated topology and a magnified section, highlighting its mesh structure.

In order to strengthen the results analysis in terms of packets, it must be noticed that similar information can be derived by analyzing the average throughput between each couple of RoIs, as in Figure 26, where data has been reported in a different way, such as the average results and the trend. Throughput is clearly lower in the AD cases. Specifically, over a period of 500 seconds, the average number of exchanged packets per RoI pair is 31.5k for healthy individuals and 22.5k for the AD subjects (independently from age and sex), approximately equal to 378Mbps and 270Mbps. The STATNET has been tuned with the above-mentioned parameters and, in Figure 26, each point represents the obtained average activity magnitude, taking into account all 48 RoIs and the patients belonging to each class, as illustrated in Figure 17.

However, this type of broad analysis provides only a static snapshot of activity and does not reflect the temporal dynamics or individual RoI-pair interactions throughout the simulation period. To address this limitation, we analyzed specific RoIs known to be affected by AD, considering the regions involved in AD progression[34].

It is known that Alzheimer affects precise regions of the brain; in particular, for the Harvard-Oxford atlas, RoIs $r^{A}_{12}$, $r^{A}_{14}$, $r^{A}_{15}$, $r^{A}_{34}$, $r^{A}_{35}$, $r^{A}_{37}$, $r^{A}_{38}$, $r^{A}_{39}$, and $r^{A}_{40}$ are mainly subject to disruptions[77]. Let us indicate the subset above as $RoI_{AD}$. To check if the proposed model reflects those effects of the disease, we show several figures related to the considered dataset, as well as the RoIs belonging to $RoI_{AD}$. Fig. 27 and 28 statistically shows the packets transmitted (TX) and received (RX) from/by $RoI_{AD}$'s nodes, for both male (blue boxplots) and female (red boxplots) over-70 healthy and diseased patients respectively. It is important to notice which is the order of magnitude and the standard deviation, in case of healthy patients. While in the healthy case, female TX activity

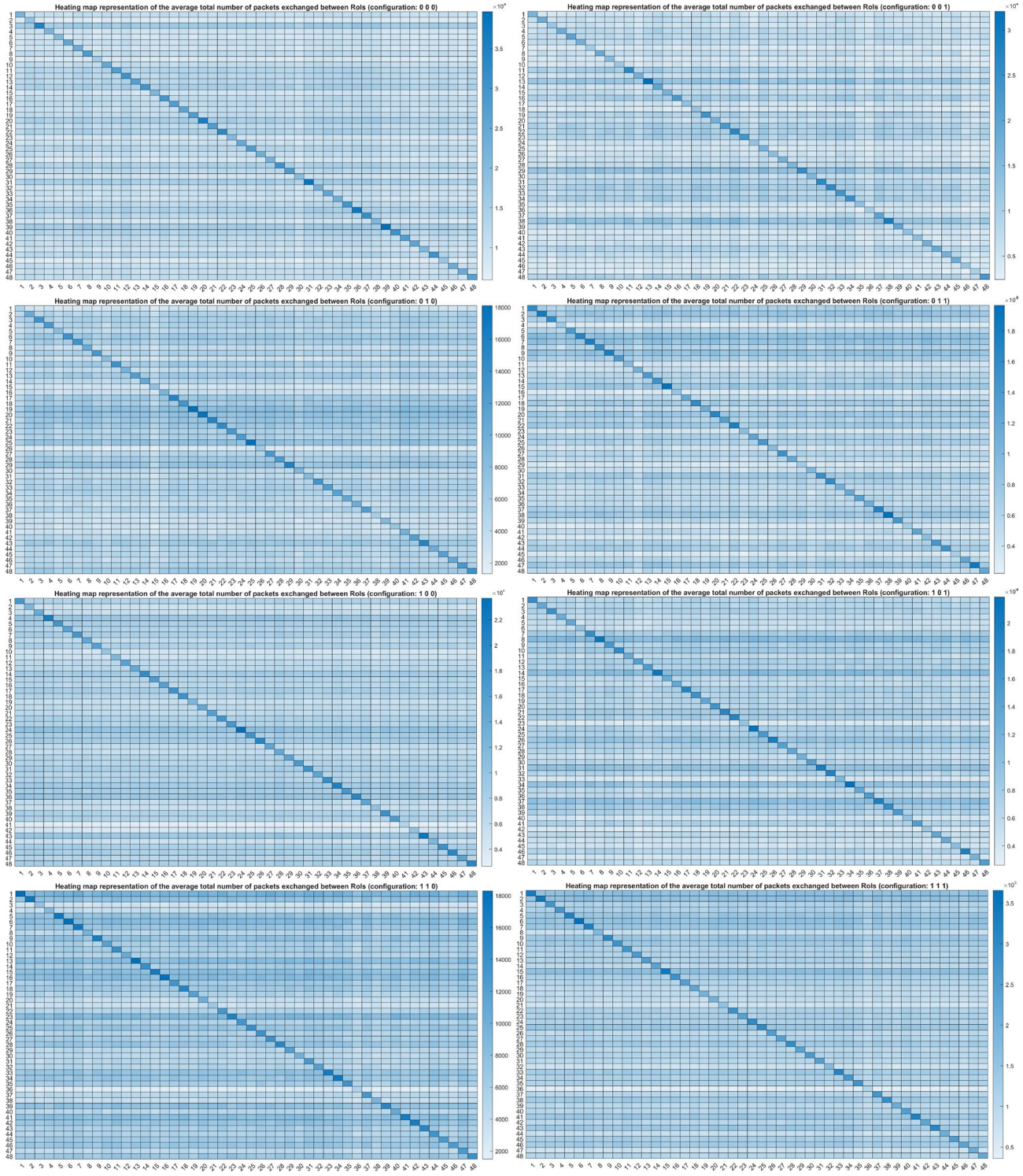


**Fig. 24**. Heatmaps showing the average total number of transmitted packets between each pair of RoIs, taking into account the patient classes illustrated in Fig. 17.

is slightly higher than male data transmissions, it is evident that the difference becomes less noticeable in the diseased case, as well as the amount of TX packets from nodes belonging to $RoI_{AD}$ is lower. Another evidence is related to the lowest variance in the diseased case. As regards $RoI_{AD}$'s RX activity, the equilibrium between male and female subjects is moreless maintained, with a lower variance respect to the TX trends. Also in this case, packets received by $RoI_{AD}$ nodes in the diseased case is much lower than the healthy case.

As regards the under-70 datasets, Figures 29 and 30 show the differences between healthy and diseased cases. As for the over-70 datasets, also in this case for the diseased case, the gap between male and female

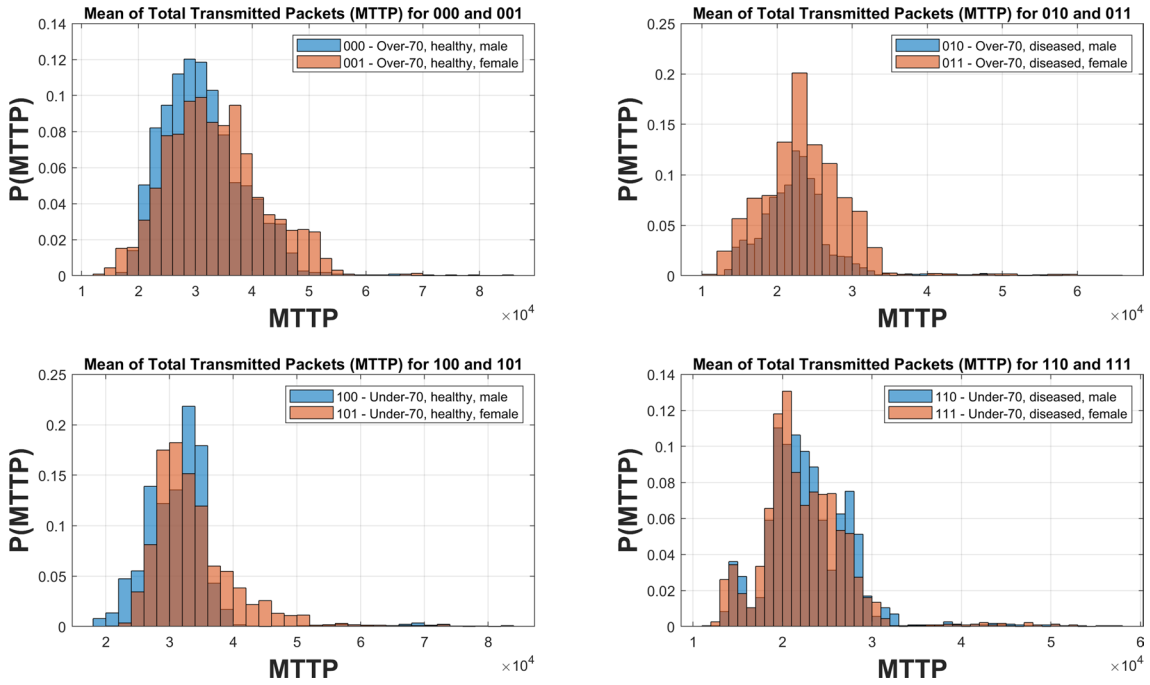


**Fig. 25**. Pdf histograms of the number of total transmitted packets (MTTP) for the 48 RoIs after 500 seconds.

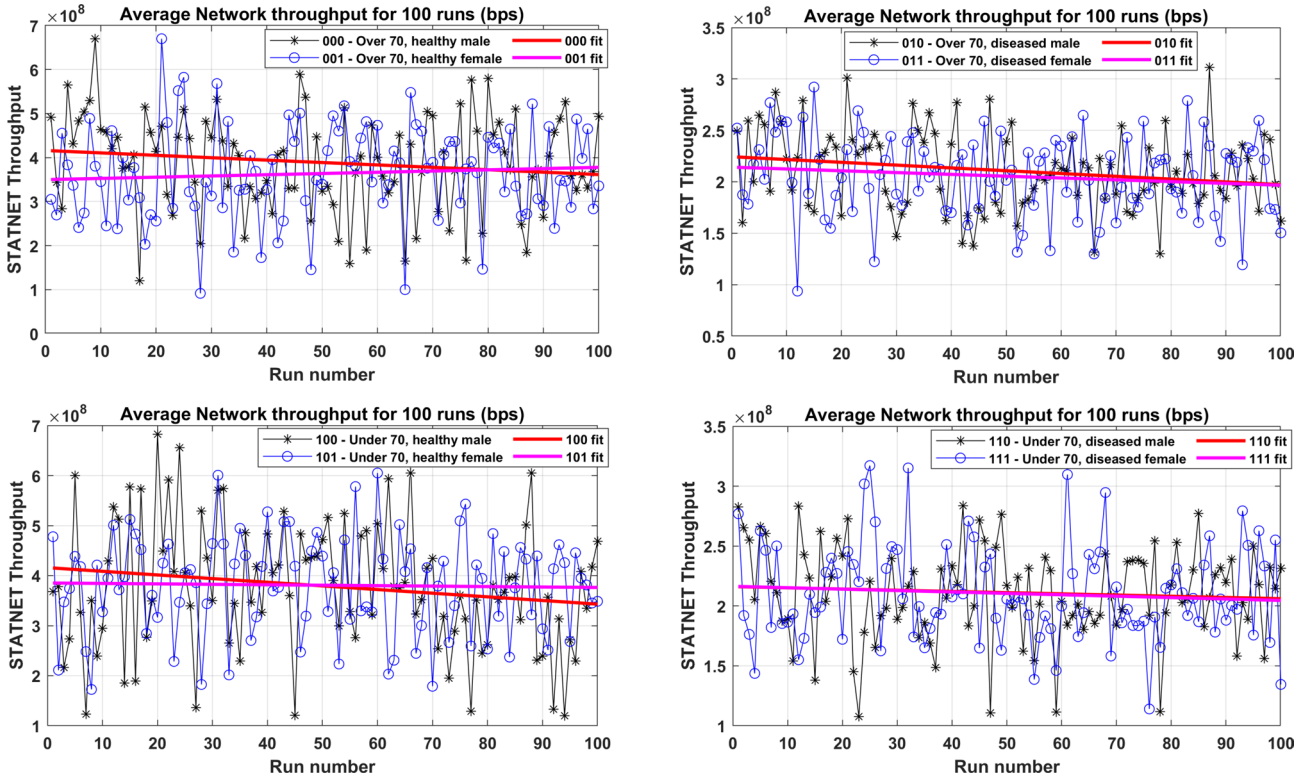


**Fig. 26**. Trend of the average throughput (bps) between each couple of STATNET nodes. Dark curves represent the average value for each round, while light lines the average trend. Values have been averaged over all healthy or diseased patients and the STATNET activity has been simulated for 500s.

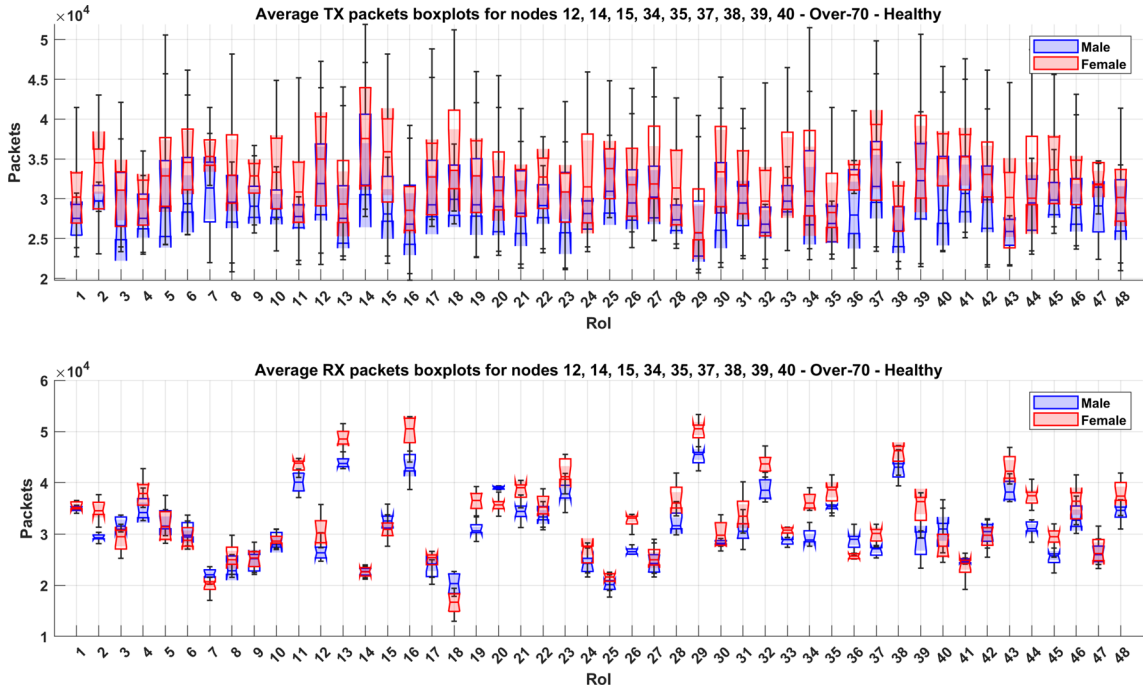


**Fig. 27**. Transmitted (TX) and received (RX) packets for over-70 healthy patients: percentiles are evaluated considering the distributions for nodes 12, 14, 15, 34, 35, 37, 38, 39, 40.

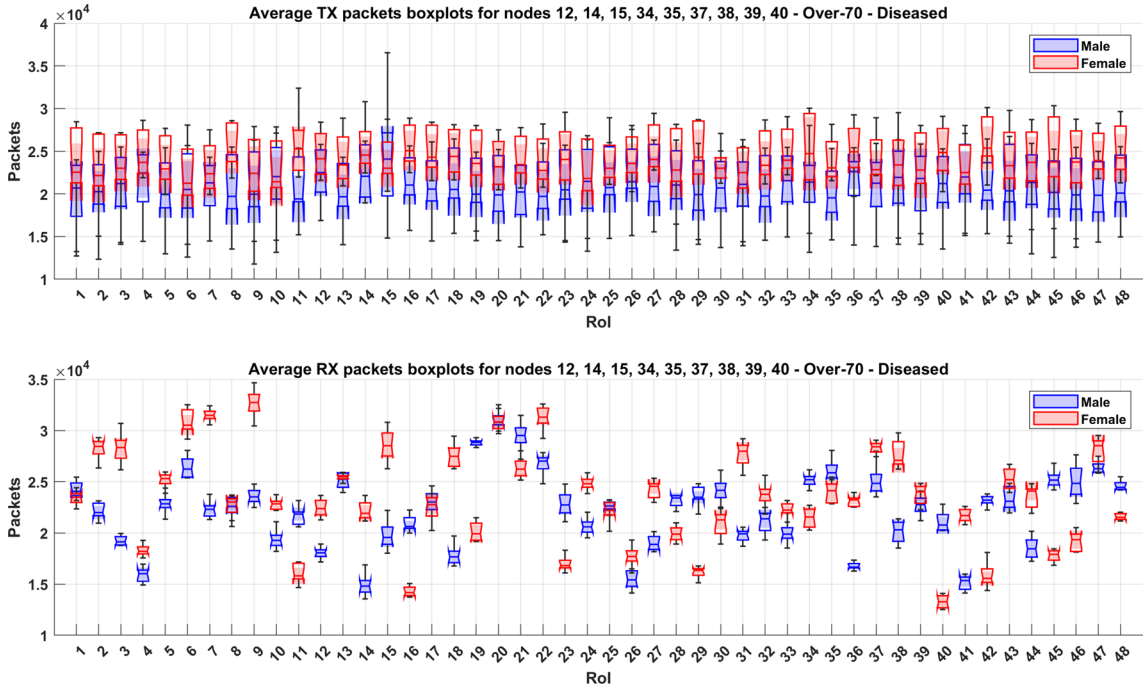


**Fig. 28**. Transmitted (TX) and received (RX) packets for over-70 diseased patients: percentiles are evaluated considering the distributions for nodes 12, 14, 15, 34, 35, 37, 38, 39, 40.

patients is less evident, with an almost complete overlapping of most values of TX packets, while the TX activity reduction is reduced, compared with the older patients. These findings suggest that in older patients there are more transmitted packets, probably due to the needing of higher signals between different brain areas and the effects of the disease are higher in terms of TX activity reduction.

After the above-shown qualitative analysis, it is essential to emphasize also the variation in the trends of the TX and RX packets at the lobes-level, an aspect not addressed by works in the existing literature. So, we conclude

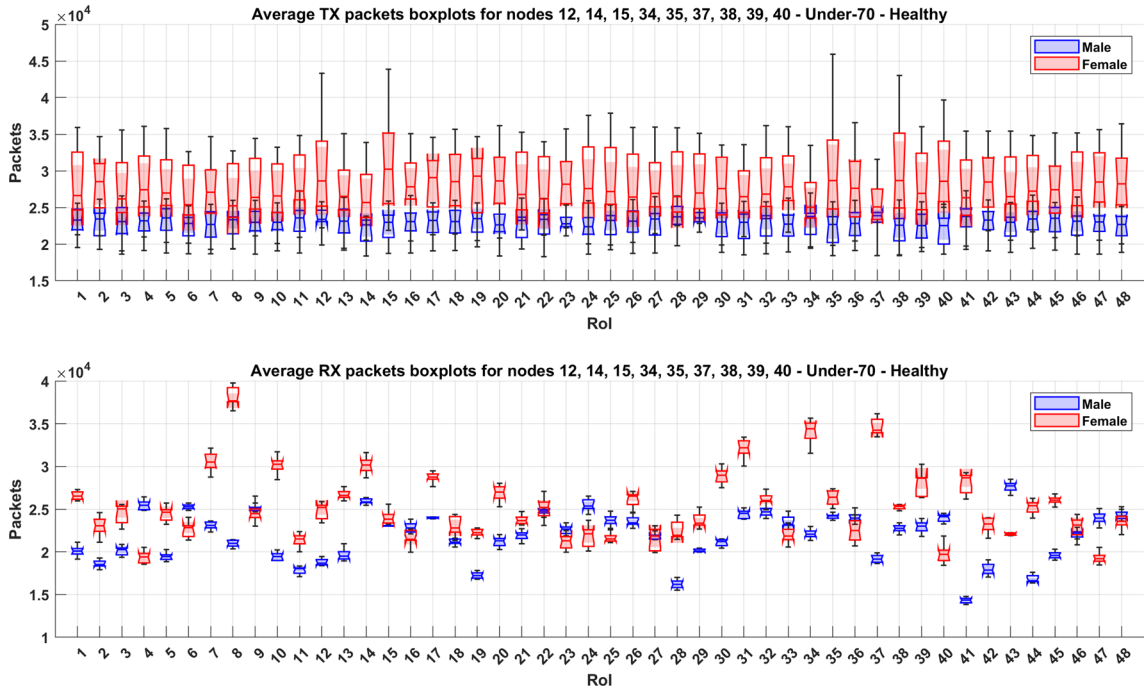


**Fig. 29**. Transmitted (TX) and received (RX) packets for under-70 healthy patients: percentiles are evaluated considering the distributions for nodes 12, 14, 15, 34, 35, 37, 38, 39, 40.

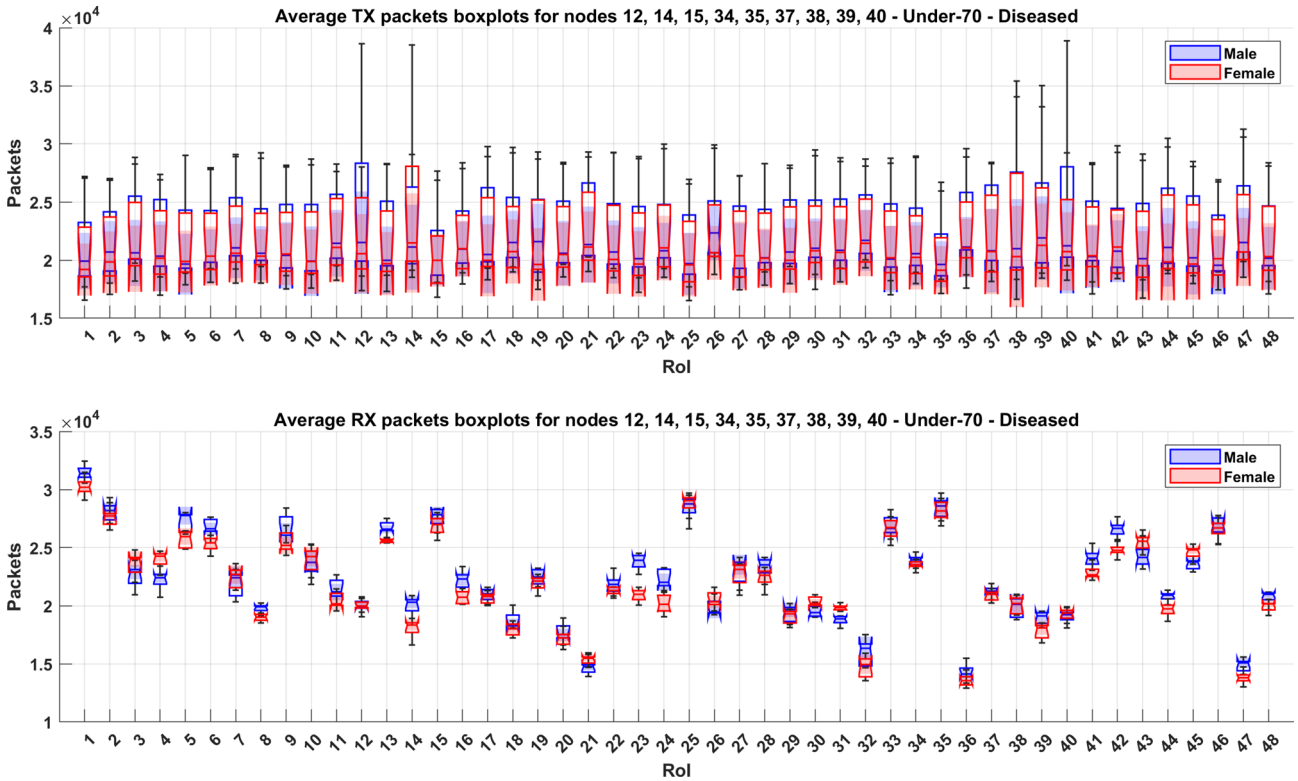


**Fig. 30**. Transmitted (TX) and received (RX) packets for under-70 diseased patients: percentiles are evaluated considering the distributions for nodes 12, 14, 15, 34, 35, 37, 38, 39, 40.

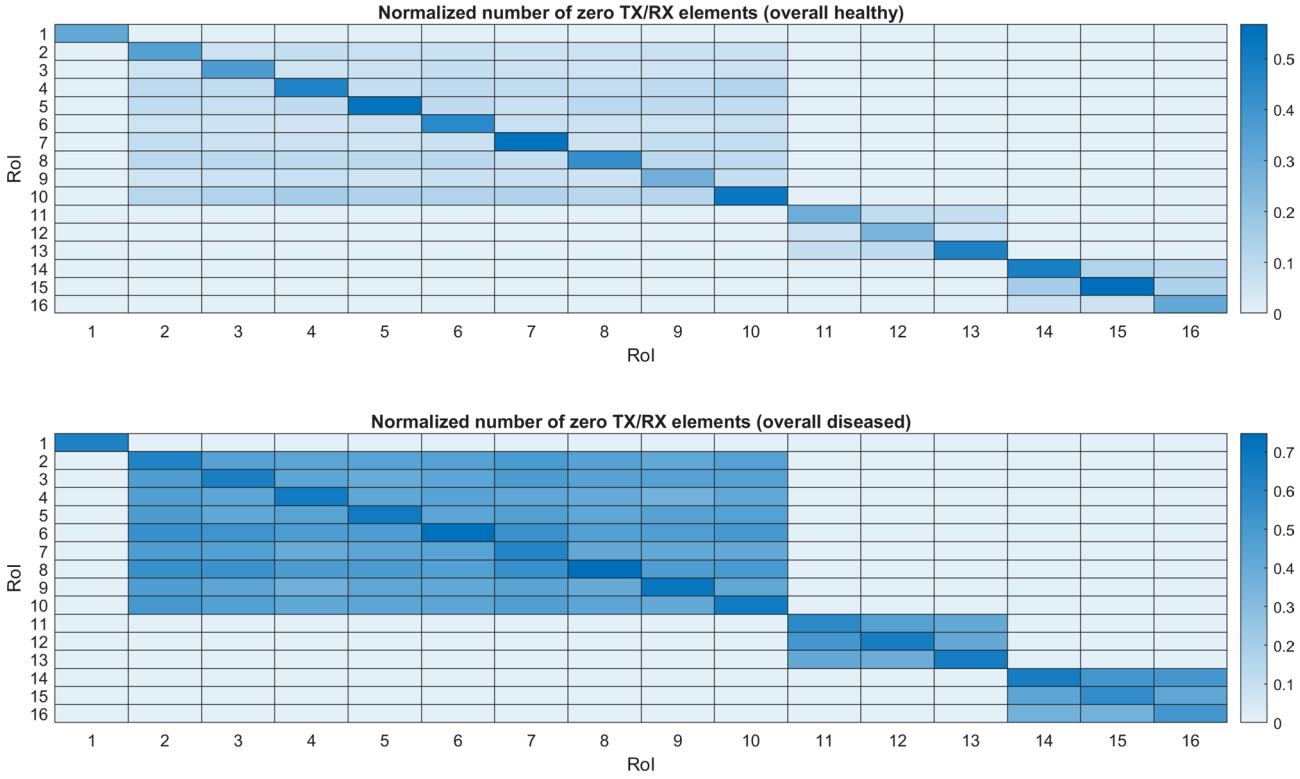


**Fig. 31**. Heatmap representation of normalized number of time windows exhibiting null TX/RX activity for the set $\{2\}$. Note that the x-axis and y-axis are labeled sequentially from 1 to 16, corresponding to the indexed positions of the elements in the original set [2, 8, 9, 10, 11, 12, 13, 14, 15, 16, 37, 38, 39, 44, 45, 46]. The upper map refers to healthy individuals, while the other one refers to diseased individuals.

our analysis by applying the following RoIs split rule and considering the anatomic proximity (numbering of RoIs from the Harvard-Oxford):

- $\{1\} = [1, 3, 4, 5, 6, 7, 25, 26, 33, 41, 42]$;
- $\{2\} = [2, 8, 9, 10, 11, 12, 13, 14, 15, 16, 37, 38, 39, 44, 45, 46]$;
- $\{3\} = [17, 18, 19, 20, 21, 31, 43]$;
- $\{4\} = [22, 23, 24, 32, 36, 40, 47, 48]$;
- $\{5\} = [27, 28, 29, 30, 34, 35]$.

We evaluate the ratio between the number of $W_q$ intervals exhibiting null TX or RX activity and the total number of $W_q$ intervals for the aggregated sets (full healthy and full diseased). We observed significant differences between the two sets, as reported in Fig. 31.

## Conclusions and future work

Exploring the human brain through a biological model inspired by clustered telecommunication networks may offer new insights into large-scale neuronal communications in the human brain. The present study introduces a framework for examining the relationship between functional connectivity and information integration in the context of human behavior. It also investigates how these communication processes may be altered or disrupted by neurodegenerative diseases.

This article presents a preliminary approach in biological brain modeling based on classic wireless and wired telecommunications theories. Our work is a detailed proof of concept with a theoretical model and its validation via data of functional connectivity in a selected group of patients. Specifically, we describe the interactions between neuronal masses within brain lobes, modeling the communication channels as subject to brain activity. A conceptual parallel between neural signaling and electromagnetic propagation phenomena is outlined, and initial results from a simulated model are presented. In future work, we aim to derive a more accurate representation of connection weights, contingent on the availability of direct measurements from biological material (e.g., organoids, stem cells, neuronal cultures). Our interdisciplinary approach, integrating complex network physics, telecommunications models, and biological cell tests, seeks to improve understanding of brain-network communications. This, in turn, could support the development of therapeutic strategies in the domain of precision medicine.

## Data availability

This study used data from the Alzheimer's Disease Neuroimaging Initiative (ADNI) database[48]. In accordance with ADNI guidelines, we declare that the investigators within the ADNI contributed to the design and implementation of ADNI and/or provided data but did not participate in the analysis or writing of this report. A complete listing of ADNI investigators can be found at the URL[78]. The data that support the findings of this study are available from the ADNI dataset, but restrictions apply to the availability of these data, which were used under license for the current study, and so are not publicly available. The main results (data series, matrices and workspaces) obtained by the authors are available at https://github.com/medusamedusa/fMRI_telecommunications.

Received: 25 September 2025; Accepted: 23 April 2026
Published online: 28 April 2026

## References

1. Yu, R. et al. Outcome prediction of unconscious patients based on weighted sparse brain network construction. *IEEE J. Biomed. Health Inform.* 11. https://doi.org/10.1109/JBHI.2022.3218652 (2023).
2. Yu, Z. et al. Emergent inference of hidden Markov models in spiking neural networks through winner-take-all. *IEEE Trans. Cybern.* **50**, 1144–1155. https://doi.org/10.1109/TCYB.2018.2871144 (2020).
3. Pathak, A., Roy, D. & Banerjee, A. Whole-brain network models: From physics to bedside. *Front. Comput. Neurosci.* **16**, 866517. https://doi.org/10.3389/fncom.2022.866517 (2022).
4. Zilles, K. Brodmann: A pioneer of human brain mapping—His impact on concepts of cortical organization. *Brain* **141**, 3262–3278. https://doi.org/10.1093/brain/awy273 (2018).
5. Bassett, D. S. & Sporns, O. Network neuroscience. *Nat. Neurosci.* **20**, 353–364. https://doi.org/10.1038/nn.4502 (2017).
6. Bassett, D. S. & Bullmore, E. T. Human brain networks in health and disease. *Curr. Opin. Neurol.* **22**, 340–347. https://doi.org/10.1097/WCO.0b013e32832d93dd (2009).
7. Chan, M. Y. et al. Resting-state network topology differentiates task signals across the adult life span. *J. Neurosci.* **37**, 2734–2745. https://doi.org/10.1523/JNEUROSCI.2406-16.2017 (2017).
8. Royer, J. et al. Epilepsy and brain network hubs. *Epilepsia* **63**, 537–550. https://doi.org/10.1111/epi.17171 (2022).
9. Rogers, B. P. et al. Assessing functional connectivity in the human brain by fMRI. *Magn. Reson. Imaging* **25**, 1347–1357. https://doi.org/10.1016/j.mri.2007.03.007 (2007).
10. Kim, S. K. & Kim, S. Brain-inspired method for hyper-connected and distributed intelligence. Proc. Int. Conf. Artif. Intell. Inf. Commun. (ICAIIC), 657–660 (2020). https://doi.org/10.1109/ICAIIC48513.2020.9065226
11. Kurashige, H. & Kaneko, J. Correspondence between the video-learning deep neural networks and EEG brain activity during naturalistic video viewing. Proc. 7th Int. Conf. Intell. Inform. Biomed. Sci. (ICIIBMS), 200–207 (2022). https://doi.org/10.1109/ICIIBMS55689.2022.9971704
12. Akyildiz, I. F. et al. Microbiome-gut-brain axis as a biomolecular communication network for the internet of bio-nanothings. *IEEE Access* **7**, 136161–136175. https://doi.org/10.1109/ACCESS.2019.2942312 (2019).
13. Fajar, A. et al. Reconstructing and resizing 3D images from DICOM files. *J. King Saud Univ. Comput. Inf. Sci.* **34**, 3517–3526. https://doi.org/10.1016/j.jksuci.2020.12.004 (2022).
14. ADNI dataset. Available at: https://adni.loni.usc.edu/
15. Brown, C. A. et al. Development, validation and application of a new fornix template for studies of aging and preclinical Alzheimer's disease. *NeuroImage. Clin.* **13**, 106–115. https://doi.org/10.1016/j.nicl.2016.11.024 (2017).
16. Desikan, R. S. et al. An automated labeling system for subdividing the human cerebral cortex on MRI scans into gyral based regions of interest. *NeuroImage* **31**, 968–980. https://doi.org/10.1016/j.neuroimage.2006.01.021 (2006).
17. Amunts, K. et al. A 3D probabilistic atlas of the human brain's cytoarchitecture. *Science* **369**, 988–992. https://doi.org/10.1126/science.abb4588 (2020).
18. Warrington, S. et al. XTRACT: Standardised protocols for automated tractography in the human and macaque brain. *Neuroimage* **217**, 116923. https://doi.org/10.1016/j.neuroimage.2020.116923 (2020).
19. Lei, B. et al. Neuroimaging retrieval via adaptive ensemble manifold learning for brain disease diagnosis. *IEEE J. Biomed. Health Inform.* **23**, 1661–1673. https://doi.org/10.1109/JBHI.2018.2872581 (2019).
20. Brainder. The NIFTI file format. Available at: https://brainder.org/2012/09/23/the-nifti-file-format/ (Accessed: April 21, 2024).
21. Li, X. et al. The first step for neuroimaging data analysis: DICOM to NIfTI conversion. *J. Neurosci. Methods* **264**, 47–56. https://doi.org/10.1016/j.jneumeth.2016.03.001 (2016).
22. Brainlife. fMRI networks. Available at: https://brainlife.io/docs/tutorial/networkneuroscience-functional/ (Accessed: Oct 11, 2024).
23. Doucet, G. E. et al. Transdiagnostic and disease-specific abnormalities in the default-mode network hubs in psychiatric disorders: A meta-analysis of resting-state functional imaging studies. *Eur. Psychiatry* **63**, e57. https://doi.org/10.1192/j.eurpsy.2020.57 (2020).
24. Lucci, B. The contribution of Gaetano Perusini to the definition of Alzheimer's disease. *Ital. J. Neurol. Sci.* **19**, 49–52. https://doi.org/10.1007/BF03028813 (1998).
25. Corrivetti, F., Herbet, G., Moritz-Gasser, S. & Duffau, H. Prosopagnosia induced by a left anterior temporal lobectomy following a right temporo-occipital resection in a multicentric diffuse low-grade glioma. *World Neurosurg.* **97**(756), e1-756.e5. https://doi.org/10.1016/j.wneu.2016.10.025 (2017).
26. Schummer, G. The disconnection syndrome. *Biofeedback* **37**, 157–162 (2009).
27. Heuvel, M. & Sporns, O. Network hubs in the human brain. *Trends Cogn. Sci.* **12**, 683–696. https://doi.org/10.1016/j.tics.2013.09.012 (2013).
28. Heuvel, M., Mandl, R., Stam, C., Kahn, R. & Pol, H. Aberrant frontal and temporal complex network structure in schizophrenia: A graph theoretical analysis. *J. Neurosci.* **30**, 15915–15926. https://doi.org/10.1523/JNEUROSCI.2874-10.2010 (2010).
29. Schipul, S. E., Keller, T. A. & Just, M. A. Inter-regional brain communication and its disturbance in autism. *Front. Syst. Neurosci.* **5**, 10. https://doi.org/10.3389/fnsys.2011.00010 (2011).
30. Just, M. A., Cherkassky, V. L., Keller, T. A., Kana, R. K. & Minshew, N. J. Functional and anatomical cortical underconnectivity in autism: Evidence from an fMRI study of an executive function task and corpus callosum morphometry. *Cereb. Cortex* **17**, 951–961. https://doi.org/10.1093/cercor/bhl006 (2007).
31. Yu, K. et al. Measuring functional connectivity in patients with strabismus using stationary functional magnetic resonance imaging: a resting-state network study. *Acta Radiol.* **63**, 110–121. https://doi.org/10.1177/0284185120983978 (2022).
32. Jin, H., Chen, R. B., Zhong, Y. L., Lai, P. H. & Huang, X. Effect of impaired stereoscopic vision on large-scale resting-state functional network connectivity in comitant exotropia patients. *Front. Neurosci.* **16**, 833937. https://doi.org/10.3389/fnins.2022.833937 (2022).
33. Badhwar, A. et al. Resting-state network dysfunction in Alzheimer's disease: A systematic review and meta-analysis. *Alzheimers Dement (Amst)* **8**, 73–85. https://doi.org/10.1016/j.dadm.2017.03.007 (2017).

34. Fathian, A., Jamali, Y. & Raoufy, M. The trend of disruption in the functional brain network topology of Alzheimer's disease. *Sci. Rep.* **12**, 14998. https://doi.org/10.1038/s41598-022-18987-y (2022).
35. Seeley, W. Mapping neurodegenerative disease onset and progression. *Cold Spring Harb. Perspect. Biol.* **9**, a023622. https://doi.org/10.1101/cshperspect.a023622 (2017).
36. Li, C. et al. Model-based image updating for brain shift in deep brain stimulation electrode placement surgery. *IEEE Trans. Biomed. Eng.* **67**, 3542–3552. https://doi.org/10.1109/TBME.2020.2990669 (2020).
37. Zhan, X. et al. Rapid estimation of entire brain strain using deep learning models. *IEEE Trans. Biomed. Eng.* **68**, 3424–3434. https://doi.org/10.1109/TBME.2021.3073380 (2021).
38. Stouffer, K. M. et al. Cross-modality mapping using image varifolds to align tissue-scale atlases to molecular-scale measures with application to 2D brain sections. *Nat. Commun.* **15**, 47883. https://doi.org/10.1038/s41467-024-47883-4 (2024).
39. Dworetsky, A. et al. Two common and distinct forms of variation in human functional brain networks. *Nat. Neurosci.* **27**, 1452–1464. https://doi.org/10.1038/s41593-024-01618-2 (2024).
40. beim Graben, P., Liebscher, T. & Kurths, J. Neural and cognitive modeling with networks of leaky integrator units. In *Lectures in Supercomputational Neuroscience: Dynamics in Complex Brain Networks* 195–223 (Springer, 2008). https://doi.org/10.1007/978-3-540-73159-7_7.
41. Sardi, S., Vardi, R., Sheinin, A., Goldental, A. & Kanter, I. New types of experiments reveal that a neuron functions as multiple independent threshold units. *Sci. Rep.* **7**, 18036. https://doi.org/10.1038/s41598-017-18363-1 (2017).
42. Mannone, M., Fazio, P. & Marwan, N. Modeling a neurological disorder as the result of an operator acting on the brain: A first sketch based on network channel modeling. *Chaos* **34**, 051103. https://doi.org/10.1063/5.0199988 (2024).
43. Vaiana, M. & Muldoon, S. Multilayer brain networks. *J. Nonlinear Sci.* **30**, 2147–2169. https://doi.org/10.1007/s00332-017-9436-8 (2017).
44. Thanh-Nam, T., Thoai Phu, V., Fazio, P. & Voznak, M. SWIPT Model adopting a PS framework to aid IoT networks inspired by the emerging cooperative NOMA technique. *IEEE Access* **9**, 61489–61512. https://doi.org/10.1109/ACCESS.2021.3074351 (2021).
45. Wu, S. et al. A general 3-D non-stationary 5G wireless channel model. *IEEE Trans. Commun.* **66**, 3065–3078. https://doi.org/10.1109/TCOMM.2017.2779128 (2018).
46. Han, C. et al. Terahertz wireless channels: A holistic survey on measurement, modeling, and analysis. *IEEE Commun. Surv. Tutor.* **24**, 1670–1707. https://doi.org/10.1109/COMST.2022.3182539 (2022).
47. Santamaria, A. F., Sottile, C. & Fazio, P. PAMTree: Partitioned multicast tree protocol for efficient data dissemination in a VANET environment. *Int. J. Distrib. Sens. Netw.* https://doi.org/10.1155/2015/431492 (2015).
48. The ADNI dataset http://adni.loni.usc.edu/data-samples/access-data/
49. The ADNI dataset, how to access data, http://adni.loni.usc.edu/data-samples/access-data/https://adni.loni.usc.edu/wp-content/themes/freshnews-dev-v2/documents/clinical/ADNI-2_Protocol.pdf
50. Dale, H. Pharmacology and nerve-endings (Walter Ernest Dixon memorial lecture): Section of therapeutics and pharmacology. *Proc. R. Soc. Med.* **28**(3), 319–332. https://doi.org/10.1177/003591573502800330 (1934).
51. Amunts, K. et al. Julich-Brain: A 3D probabilistic atlas of the human brain's cytoarchitecture. *Science* **369**, 988–992. https://doi.org/10.1126/science.abb4588 (2020).
52. Dadi, K. et al. Fine-grain atlases of functional modes for fMRI analysis. *Neuroimage* **221**, 117126. https://doi.org/10.1016/j.neuroimage.2020.117126 (2020).
53. Jung, W. et al. EAG-RS: A novel explainability-guided ROI-selection framework for ASD diagnosis via inter-regional relation learning. *IEEE Trans. Med. Imaging* **43**, 1400–1411. https://doi.org/10.1109/TMI.2023.3337362 (2024).
54. Wang, M. et al. SNR improved digital-PCM radio-over-fiber scheme supporting 65536 QAM for mobile fronthaul. *IEEE Photon. Technol. Lett.* **35**, 825–828. https://doi.org/10.1109/LPT.2023.3284456 (2023).
55. Oliver, B. M., Pierce, J. R. & Shannon, C. E. The philosophy of PCM. *Proc. IRE* **36**, 1324–1331. https://doi.org/10.1109/JRPROC.1948.231941 (1948).
56. Tan, L. & Jiang, J. Waveform quantization and compression. In *Digital Signal Processing* Third Edition 475–527 (Elsevier, 2019). https://doi.org/10.1016/B978-0-12-815071-9.00010-5.
57. Miller, L. S. & Childers, D. Markov processes. In *Probability and Random Processes* Second Edition 383–428 (Elsevier, 2012). https://doi.org/10.1016/B978-0-12-386981-4.50012-6.
58. Geerligs, L., Cam, C. & Henson, R. N. Functional connectivity and structural covariance between regions of interest can be measured more accurately using multivariate distance correlation. *Neuroimage* **135**, 16–31. https://doi.org/10.1016/j.neuroimage.2016.04.047 (2016).
59. Coniglione, M., Ballante, E., Assecondi, S. & Figini, S. A New Optimized Clustering Applied to Sparse Spearman Correlation Estimation Network to Investigate Cognition. Scientific Meeting of the Italian Statistical Society, Springer. https://doi.org/10.1007/978-3-031-96303-2_79. (2025).
60. Bressler, D., Spotswood, N. & Whitney, D. Negative BOLD fMRI response in the visual cortex carries precise stimulus-specific information. *PLoS. One* **2**, e410. https://doi.org/10.1371/journal.pone.0000410 (2007).
61. Carpentries. Anatomy of a NIfTI. Available at: https://carpentries-incubator.github.io/SDC-BIDS-IntroMRI/anatomy-of-nifti.html
62. Mesner, O. C. & Shalizi, C. R. Conditional mutual information estimation for mixed, discrete and continuous data. *IEEE Trans. Inf. Theory* **67**, 464–484. https://doi.org/10.1109/TIT.2020.3024886 (2021).
63. Zhang, W. et al. Mutual information better quantifies brain network architecture in children with epilepsy. *Comput. Math. Methods Med.* **2018**, 6142898. https://doi.org/10.1155/2018/6142898 (2018).
64. Mahmoudi, A. & Jemielniak, D. Proof of biased behavior of normalized mutual information. *Sci. Rep.* **14**, 59073. https://doi.org/10.1038/s41598-024-59073-9 (2024).
65. Sheng, A. et al. Constructing temporal networks with bursty activity patterns. *Nat. Commun.* **14**, 42868. https://doi.org/10.1038/s41467-023-42868-1 (2023).
66. Heeger, D. Poisson model of spike generation. Handout, Stanford University. https://doi.org/10.1371/journal.pcbi.1008261 (2000).
67. Herculano-Houzel, S. The human brain in numbers: A linearly scaled-up primate brain. *Front. Hum. Neurosci.* https://doi.org/10.3389/neuro.09.031.2009 (2009).
68. V. Braitenberg, A. Schüz. Cortex: Statistics and Geometry of Neuronal Connectivity. Springer Verlag (1998), 2nd edition. Chapters 5 and 6. https://doi.org/10.1007/978-3-662-03733.
69. Morales-Gregorio, A., Van Meegen, A. & Van Albada, S. J. Ubiquitous lognormal distribution of neuron densities in mammalian cerebral cortex. *Cereb. Cortex* https://doi.org/10.1093/cercor/bhad160 (2023).
70. Collins, C. E. et al. Neuron densities vary across and within cortical areas in primates. *Proc. Natl. Acad. Sci. U. S. A.* **107**(36), 15927–15932. https://doi.org/10.1073/pnas.1010356107 (2010).
71. Ross, P. et al. Cerebral cortex: An MRI-based study of volume and variance with age and sex. *J. Clin. Neurosci.* **13**(1), 60–72. https://doi.org/10.1016/j.jocn.2005.02.013 (2006).
72. Korhonen, O. et al. Consistency of regions of interest as nodes of fMRI functional brain networks. *Netw. Neurosci.* https://doi.org/10.1162/NETN_a_00013 (2017).
73. Szymanski, T. H. Max-flow min-cost routing in a future-Internet with improved QoS guarantees. *IEEE Trans. Commun.* **61**, 1485–1497. https://doi.org/10.1109/TCOMM.2013.020713.110882 (2013).

74. Bartol, T. M. Jr. et al. Nanoconnectomic upper bound on the variability of synaptic plasticity. *eLife* **4**, e10778. https://doi.org/10.7554/eLife.10778 (2015).
75. Micheva, K. D. et al. Single-synapse analysis of a diverse synapse population: Proteomic imaging methods and markers. *Neuron* **68**, 639–653. https://doi.org/10.1016/j.neuron.2010.09.024 (2010).
76. Frankland, P. W., Josselyn, S. A. & Köhler, S. The neurobiological foundation of memory retrieval. *Nat. Neurosci.* **22**, 1576–1585. https://doi.org/10.1038/s41593-019-0493-1 (2019).
77. da Silva Filho, S. R. B. et al. Neuro-degeneration profile of Alzheimer's patients: A brain morphometry study. *Neuroimage. Clin.* **12**, 15–24. https://doi.org/10.1016/j.nicl.2017.04.001 (2017).
78. The ADNI contributor list https://adni.loni.usc.edu/wp-content/uploads/how_to_apply/ADNI_Acknowledgement_List.pdf.

## Author contributions

P.F. and M.Ma. contributed to the conceptualization of the study and the development of the methodological framework. N.M. supported the methodological design and was primarily responsible for data curation. P.R. contributed to the acquisition and organization of data and assisted with validation procedures. M.Me. and A.S. conducted the formal analyses and were involved in data visualization and interpretation. D.A. and P.R. developed and maintained the computational tools and software environment required for the study. P.F. prepared the initial draft of the manuscript with substantive input from M.Ma. and A. S. P.F., M.Ma., and P.R. revised the manuscript critically for important intellectual content. M.V. provided overall supervision, coordinated project administration, and secured funding to support the research. All authors reviewed and approved the final version of the manuscript and agree to be accountable for all aspects of the work.

## Funding

This article has been produced with the financial support of the European Union under the REFRESH – Research Excellence For REgion Sustainability and High-tech Industries project number CZ.10.03.01/00/22_003/0000048 via the Operational Programme Just Transition. The article has received also financial support from the Next Generation EU – "Age-It – Ageing Well in an Ageing Society" project (PE0000015), under the National Recovery and Resilience Plan (NRRP) – PE8 – Mission 4, C2, Intervention 1.3, CUP B83C22004880006.

## Declarations

## Competing interests

The authors declare no competing interests.

## Additional information

**Correspondence** and requests for materials should be addressed to P.F.

**Reprints and permissions information** is available at www.nature.com/reprints.

**Publisher's note** Springer Nature remains neutral with regard to jurisdictional claims in published maps and institutional affiliations.